2nd EF Conference in

TURBULENT HEAT

TRANSFER

Manchester, UK 1998

Measured   Predicted

ENGINEERING FOUNDATION

REPORT DOCUMENTATION PAGE

Form Approved OMB No. 0704-0188

1. AGENCY USE ONLY (Leave blank)	2. REPORT DATE	3. REPORT TYPE AND DATES COVERED
	1998	Conference Proceedings

4. TITLE AND SUBTITLE

2nd EF Conference in Turbulent Heat Transfer

5. FUNDING NUMBERS

F61775-98-WE001

6. AUTHOR(S)

Conference Committee

7. PERFORMING ORGANIZATION NAME(S) AND ADDRESS(ES)

The University of Manchester Institute (UMIST)
PO Box 88 (Dept of Mechanical Engineering)
Manchester M60 1QD
United Kingdom

8. PERFORMING ORGANIZATION REPORT NUMBER

N/A

9. SPONSORING/MONITORING AGENCY NAME(S) AND ADDRESS(ES)

EOARD
PSC 802 BOX 14
FPO 09499-0200

10. SPONSORING/MONITORING AGENCY REPORT NUMBER

CSP 98-1012

11. SUPPLEMENTARY NOTES

Three volumes (one appears to be data omitted from one of the other two volumes).

12a. DISTRIBUTION/AVAILABILITY STATEMENT

Approved for public release; distribution is unlimited.

12b. DISTRIBUTION CODE

A

13. ABSTRACT (Maximum 200 words)

The Final Proceedings for Turbulent Heat Transfer II, 31 May 1998 - 5 June 1998

This is an interdisciplinary conference. Topics include Momentum & Heat Transfer in Simple Shear with/without Velocity Extrema; Low-Reynolds-Number Phenomena; Effects of Curvature, Rotation, Buoyancy on Heat Transfer; Impingement & Separated Flows; Effects of Streamwise Vortices on Heat Transfer; Control of Turbulent Flow; Transport across Fluid-Fluid Interfaces; Progress in Instrumentation; Review of CFD Test Cases/Inquests.

14. SUBJECT TERMS

Heat Transfer, Numerical Simulation, CFD

15. NUMBER OF PAGES

Too many to count

16. PRICE CODE

N/A

17. SECURITY CLASSIFICATION OF REPORT	18. SECURITY CLASSIFICATION OF THIS PAGE	19. SECURITY CLASSIFICATION OF ABSTRACT	20. LIMITATION OF ABSTRACT
UNCLASSIFIED	UNCLASSIFIED	UNCLASSIFIED	UL

NSN 7540-01-280-5500

Standard Form 298 (Rev. 2-89)
Prescribed by ANSI Std. 239-18
298-102

2nd International Conference

on

TURBULENT HEAT TRANSFER

Manchester

May 31 - June 4, 1998

Organized by UMIST and the University of Manchester

In collaboration with

ASME Heat Transfer Division

The Engineering Foundation
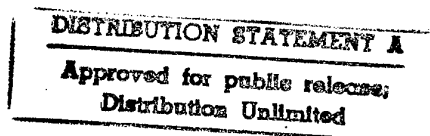
Sponsorship of THT-2

The Organizing Committee expresses its sincere appreciation to the following organizations for their support of this conference:

UK Health & Safety Executive
US Air Force
US Army
ABB
Electricité de France
Magnox Electric
Nuclear Electric
Shell Research, Amsterdam

Organizing Committee

Brian Launder, Chairman
Derek Jackson, Co-Chairman
Pepe Humphrey, Nobu Kasagi
Al Ortega, Frank Schmidt

Local Arrangements Committee

Pei An, Brian Axcell, John Byrne
Tim Craft, Shui-Sheng He,
Hector Iacovides, David Jackson
Derek Jackson, Catherine King,
Brian Launder

Scientific Committee

G Bergeles, K Bremhorst, J Coupland
J K Eaton, M Fiebig, K Hanjalic, J Hannis
B V Johnson, T V Jones, D Laurence,
Y Nagano, J M Owen, S Sarkar, A M Savill,
R M C So, K Suzuki, R Viskanta

LES AND RANSE OF TURBULENT FLOW IN TUBE BUNDLES

D. Laurence[1], P. Rollet-Miet[1,2]

1. EDF DER-LNH, 6 quai Watier, 78401 Chatou, France
2. LMFA UMR CNRS 5509, Ecole Centrale de Lyon, 69131 Ecully, France

ABSTRACT

Large Eddy Simulation (LES) is developed in a general purpose Finite Element code. It is first shown that the standard numerical schemes developed for the Reynolds Averaged Navier Stokes Equations (RANSE) are not suitable for LES. Validation of the final centred and collocated scheme is carried out for grid turbulence and channel flow. The same code is then applied to a complex flow that has challenged RANSE modelling for years: a crossflow in a tube bundle. In opposition to such models, the LES yields results in good agreement with the experimental data of Simonin et al., including for the Reynolds stresses.

1. INTRODUCTION

Large Eddy Simulation (LES) has long been restricted to academic flows (homogeneous or channel flows), while models for Reynolds Averaged Navier Stokes Equations (RANSE) are commonly applied to three-dimensional flows in complex geometries. Some fairly complex domains are simulated by LES : flow around a cube or a square cylinder (1). However LES simulations require high mesh refinements near the body and induces in structured meshes a very high number of mesh points. The advantage of unstructured grids is to allow local mesh refinement (2). But on the other hand, the highly accurate schemes used for LES (Pseudo-spectral or Padé schemes) are applicable only to cartesian grids. Only two applications of LES code on unstructured grids for incompressible fluid developments are known (2) & (3). We present here the development of a LES code for incompressible fluid through a Finite Element Method (4). This LES version is based on the N3S code developed by Chabard et al.(5).

The organisation of this paper is as follows. The numerical issues which were explored are described in Sec. 2. The effect of numerical method on LES of channel flow is analysed in Sec. 3. The final numerical tool is applied to tube bundle flow in Sec. 4.

2. NUMERICAL ISSUES

In opposition to the Reynolds Averaged Navier-Stokes Equations (RANSE), with LES one explicitly computes the large scales of motion and introduces a model for only the small motions. LES is based upon the application of a spatial filtering operation (denoted by a bar) to the three-dimensional unsteady Navier-Stokes equations. We assume, and subsequently check from energy spectra, that the filtering is induced by the numerical scheme and the computational grid.

Let $\overline{u}$ the (filtered) velocity of large scale motion. The subgrid-scale stresses (SGS) τ_{ij} result from the influence of unresolved scales on large scales, and are defined by $\tau_{ij} = \overline{u_i u_j} - \overline{u}_i \overline{u}_j$

The filtered Navier-Stokes equations:

$$\begin{cases} \dfrac{\partial \overline{u}_i}{\partial t} + \dfrac{\partial \overline{u}_i \overline{u}_j}{\partial x_j} = -\dfrac{1}{\rho} \dfrac{\partial \overline{p}}{\partial x_i} + \mu \dfrac{\partial^2 \overline{u}_i}{\partial x_i \partial x_i} - \dfrac{\partial \tau_{ij}}{\partial x_i} \\ \dfrac{\partial \overline{u}_i}{\partial x_i} = 0 \end{cases}$$

The Smagorinsky model is a simple mixing length model:

$$\tau_{ij}^d = \tau_{ij} - \frac{1}{3} \tau_{kk} \delta_{ij}$$

$$= -2 v_t \, \overline{S}_{ij} = -2 C \overline{\Delta}^2 |\overline{S}| \, \overline{S}_{ij}$$

with v_t the turbulent viscosity

and $\overline{\Delta}$ the characteristic length scale, $\overline{\Delta} = 2h$,

with h the mesh spacing for a regular mesh

$$S_{ij} = \frac{1}{2}\left(\frac{\partial u_i}{\partial x_j} + \frac{\partial u_j}{\partial x_i} \right) \text{ and } |S| = \left(2 S_{ij} S_{ij} \right)^{\frac{1}{2}}$$

$C = C_s^2$, C_s is the Smagorinsky constant

The subgrid-modelling is an important problem for LES, but we focus here on the numerical requirements of LES on unstructured grid.

2.1. Time advancement

Two different methods have been tested: the method of characteristics, and the centred Adams-Bashford, Crank-Nicholson scheme (AB-CN).

The characteristics scheme deals only with the advection step[5]and is used within a fractional time-step method. For pure advection, velocities are conserved along the characteristic curve defined by: $\dfrac{dx}{dt} = u$,

$\dfrac{dy}{dt} = v$, $\dfrac{dz}{dt} = w$. At each time step t^n, this curve is followed backwards from each node. Once the location of the fluid particle at t^{n-1} is known, the velocity is interpolated by quadratic or higher order interpolation functions. Then, the Stokes problem will be solved for this intermediate velocity field.

This approach is very attractive, because it introduces a natural upwinding and is unconditionally stable: it is used daily for k-ε calculations. For steady state problems, it has very low numerical diffusion since cubic or hermitian interpolation can be used at the end of the characteristic curve. But, for a highly unsteady flow as in LES, and since the discretised characteristics method mixes interpolation in space and time, the first order temporal interpolation results in unacceptable numerical damping. As for any upwind scheme, an artificial viscosity can be exhibited. Namely, for the characteristics method, in 1D, for a regular grid and u the advection velocity:

$$\frac{\partial f}{\partial t} \approx \frac{f_x^{n+1} - f_x^n}{\Delta t} = \frac{f_{x-u\Delta t}^n - f_x^n}{\Delta t}$$

By a Taylor expansion:

$$\frac{\partial f}{\partial t} \approx -u\frac{\partial f}{\partial x} + \upsilon_{num}\frac{\partial^2 f}{\partial x^2} + o(\Delta x, \Delta t), \text{ with}$$

$\upsilon_{num} = \frac{1}{2}u^2 \Delta t = \frac{1}{2}u c \Delta x$, c is the Courant number.

The scheme is first-order accurate in time and equivalently in space if the Courant number is prescribed, this whatever the order of the spatial interpolation at the end of the characteristic. This was identified in (6) and resolved for cartesian grids by introducing a moving frame of reference at each time step, but cannot be extended to unstructured grids.

The very classical Adams-Bashforth Crank-Nicholson (AB-CN) scheme was then chosen to evaluate the benefits of a centred scheme. It is translated by the variational formulation to:

$$\int_\Omega \rho\frac{\tilde{\mathbf{u}} - \overline{\mathbf{u}}^n}{\Delta t}\mathbf{v}\,d\Omega + \frac{1}{2}\int_\Omega (\nu + \nu_t)\nabla\tilde{\mathbf{u}}.\nabla\mathbf{v}\,d\Omega =$$
$$-\int_\Omega \overline{p}^n\nabla\mathbf{v}\,d\Omega - \frac{1}{2}\int_\Omega(\nu + \nu_t)\nabla\overline{\mathbf{u}}^n.\nabla\mathbf{v}\,d\Omega$$
$$-\frac{3}{2}C^n + \frac{1}{2}C^{n-1} + \text{boundary terms}$$

with $\tilde{\mathbf{u}}$ the velocity field after advection-diffusion step and $\mathbf{v}$ the velocity basis function.

The influence of the formulation of convective term has been investigates in detail, but not in the FEM context. Here we chose the straightforward advective formu-

lation (6): $\qquad C_i^n = \int_\Omega u_k^n \frac{\partial u_i^n}{\partial x_k}\mathbf{v}\,d\Omega$

Linear basis function are used for the variational formulation: the scheme is fourth-order accurate for the convective term and second-order for the diffusive term (8). However, to avoid the extraneous computational cost implied by the mass-matrix, this matrix is condensed on the diagonal. This provides a second-order accurate scheme. The linear analysis proves that this scheme is stable for a Courant number less than 0.2 These schemes were compared on isotropic turbulence decay. Comparison of the energy spectra with experiment do not tell much since the dynamic model automatically decreases the Smagorinsky constant if a

dissipative scheme is used (but this is only acceptable for grid turbulence). The spectral transfer function is more significant. The variation of the spectrum of turbulent kinetic energy during the advection step was evaluated on fifty samples. The averaged variation is drawn on Fig. 1 for two meshes: a coarse one (N=32 points) and a refined grid (N=64 points). The spectral analysis shows that, for homogeneous turbulent flow, the advection implies a transfer of energy from the larger structures (small wave-number k) to the smaller ones (large k). The numerical test shows that the characteristic scheme is dissipative on the mean and very dependent of the grid: the scheme is first-order accurate in space because of the highly unsteady nature of the smaller scales. On the contrary, the centred scheme effectively transfers energy from the small wave-numbers to the large ones and fairly independent of the spatial resolution.
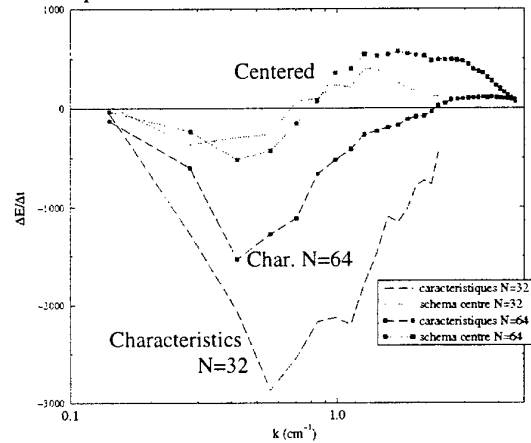

Fig. 1 Spectral transfer function T(k) in grid turbulence

We stress here that the paradoxical choices of upwind biased schemes for most RANSE computations and centred schemes for LES should be analysed in the spatial-temporal frame, and is due to the highly unsteady nature of the smallest resolved scales in LES.

2.2. Spatial discretization

Spatial discretization relies on tetrahedral elements, which enable a large flexibility in meshing. We restricted ourselves to linear shape functions. We introduce here the P1-P1 element based on collocated velocity and pressure nodes (fig.2) (hardly ever used in the F. E. literature, except to point out it's defects). The standard Finite Element discretization (used in N3S code) is the P1-isoP2 element (fig.2) based on two levels of discretization: the pressure is interpolated linearly on the macro-element, while the velocity is interpolated linearly on each sub-element.

The P1-isoP2 element verifies the well-known "inf-sup" condition, and ensures the existence and uniqueness of the solution of the discretized Stokes equation (8). On the contrary, the P1-P1 element does not verify this condition and provides spurious pressure modes.

The modes are damped out by an Arakawa correction. These modes appear mainly when the grid is generated by splitting an initially cartesian grid, but the correction is hardly necessary when the grid is fully unstructured.

● velocity   ☐ pressure

P1-isoP2 element   *P1-P1 element*
velocity filter: 2h   *v. & p. filter: 2h*
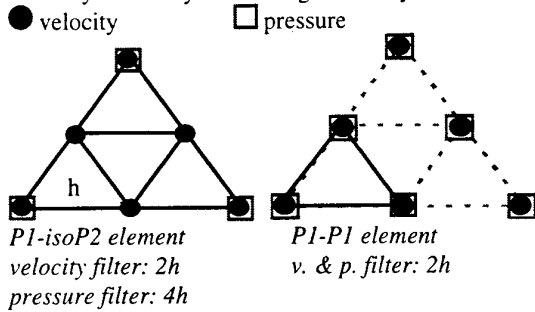*pressure filter: 4h*

Figure 2   Choice of Elements (in 2D)

Since the filter is induced implicitly by the grid and numerical scheme, it clearly appears that the filter-width is twice larger for pressure than for velocity in the case of P1-isoP2 element (see Fig. 2). The interactions between resolved and subgrid-scales are modified and it may be necessary to develop new subgrid-models. On the contrary, the filter-width are identical for velocity and pressure in the case of P1-P1 element.

The treatment of incompressibility is essential as well. Brezzi et al.(9) defined a constraint ratio: the ratio between pressure degrees of freedom and velocity degrees of freedom. In 3D, this ratio is equal to 1/3 for P1-P1 element and to 1/4 for P1-isoP2 element. Hence, the P1-isoP2 element is weakly compressible. Pelletier et al.[11] underlines one consequence of this behaviour:

$$\|u - v_h\| \le C \left\{ \underbrace{inf \|u - w_h\|}_{w_h \in V_h} + \underbrace{inf \|p - q_h\|}_{q_h \in Q_h} \right\}$$

with u and p the solutions of the continuous Stokes problem, v_h and p_h the solutions of the *discrete* problem. The precision on velocity depends both on the approximation of velocity and pressure.

A laminar test-case highlights the effect of the low resolution of pressure. In the "Taylor-Green" vortices flow, the shape of the cellular vortices remain unchanged. The analytical solution is known:

$$\begin{cases} U = -\sin(kx)\cos(ky)\,e^{-2vt} \\ V = \cos(kx)\sin(ky)\,e^{-2vt} \\ P = \frac{1}{4}[\cos(2kx) + \cos(2ky)]\,e^{-4vt} \end{cases}$$
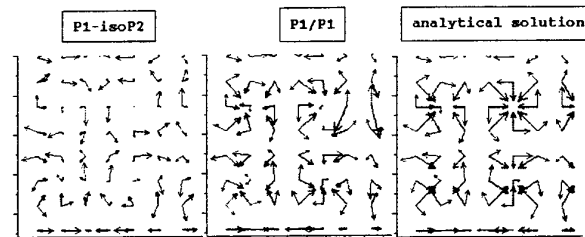

Fig. 3 Under-resolved Taylor vortices. Blue (light grey): velocities, Red (dark grey): pressure gradients.

The test is conducted with a coarse resolution: 8 points per wave-scale for velocity. After 50 time steps, the L^2 error on the velocity component u is 0.08 for P1-P1 and 0.19 for P1-isoP2. Figure 3 shows that the angles and vector amplitudes of velocity and pressure gradient are well captured by P1-P1 but not by P1-isoP2. This is very important because the energy exchanges between velocity components are driven by velocity pressure gradient product, as in the Reynolds Stress transport equations in the frame of RANS equations. The treatment of incompressibility (i.e. the pressure resolution) appears in this case more important than the respect of the inf-sup condition.

2.3. Analysis of numerical choices on LES of channel flow

Channel flow computations represent the usual benchmark for LES codes. The "minimal flow unit" was first introduced by Jimenez et al. (11): the computational box is large enough to sustain turbulence but contains only one or two wall structures (« streaks »). The streamwise, wall-normal and spanwise directions are noted respectively x, y and z.
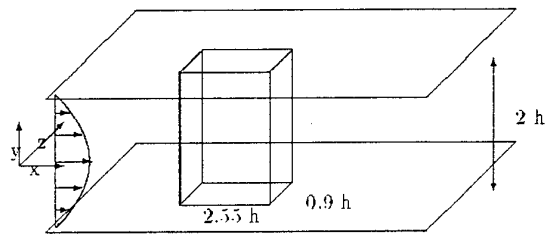
The computational domain is [2.55h, 2h, 0.9h], h being the half width of the channel. Periodicity is imposed in the x- and z-directions. The grid of our LES is composed by 157 925 nodes, dispatched in 25 identical planes in the z direction (figure 4).
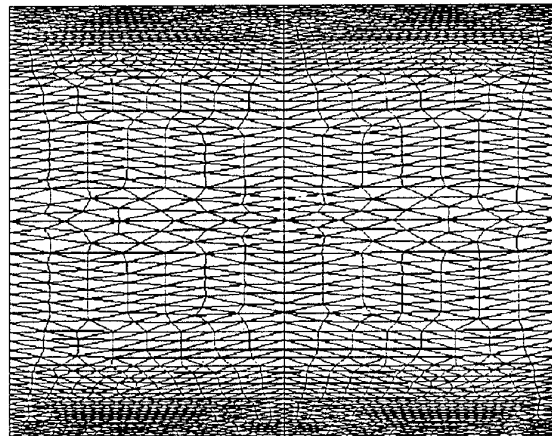

Fig 4: unstructured mesh in (x,y) plane for channel LES.

The present LES results are compared to the DNS of Boudjemadi (13). The Smagorinsky model (Cs=0.065) with a Van Driest damping function was used. Since the ratio v_t/v remains smaller than 10%, this is a quasi

DNS, i. e. a good test-case for the numerical method. Three numerical methods were tested:
A: characteristics scheme and P1-isoP2 element,
B: centred AB-CN scheme on P1-isoP2 element,
C: centred on collocated P1-P1 element.

The spatial averaging is restricted in an unstructured mesh to narrow bands parallel to the wall. Moreover, since the computational box contains few structures: a long-time integration is necessary to obtain reliable statistics. The time averaging was carried out upon 300 time units (LETOTs).

2.4. Time scheme advancement

Figure 7 shows the time history of maximum velocity. Scheme B captures high frequencies oscillations, which are characteristic of turbulent flow, whereas scheme A provides a smooth evolution due to its low accuracy in time. The rms-value of fluctuating velocities are drawn on figure 5. The numerical viscosity of scheme A (characteristics) damps the normal fluctuations, which are severely underestimated. Schemes B (centred + P1 isoP2) and C (centred + collocated) seem equally satisfactory, the latter being however somewhat superior in predicting the normal and span-wise fluctuations at the channel centre.
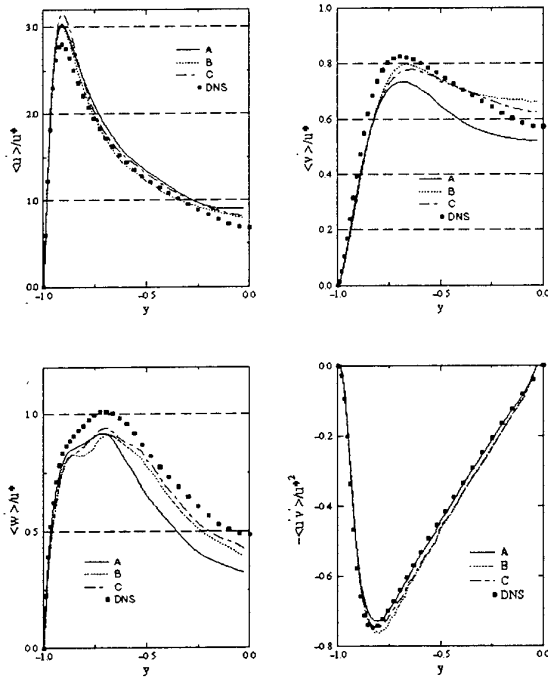

Figure 5 rms values for channel flow.

The snapshots of vorticity (not shown) and fluctuation iso-contours (fig. 6) reveal for scheme A excessively smooth structures near the wall. Since the normal fluctuations are underestimated, the turbulent structures do not migrate towards the centreline as well as for schemes B and C. Scheme « A » does not capture the essential features of this turbulent flow and will not be

used for subsequent LES simulation. Reasons for choice of scheme C instead of B is explained in the following section.
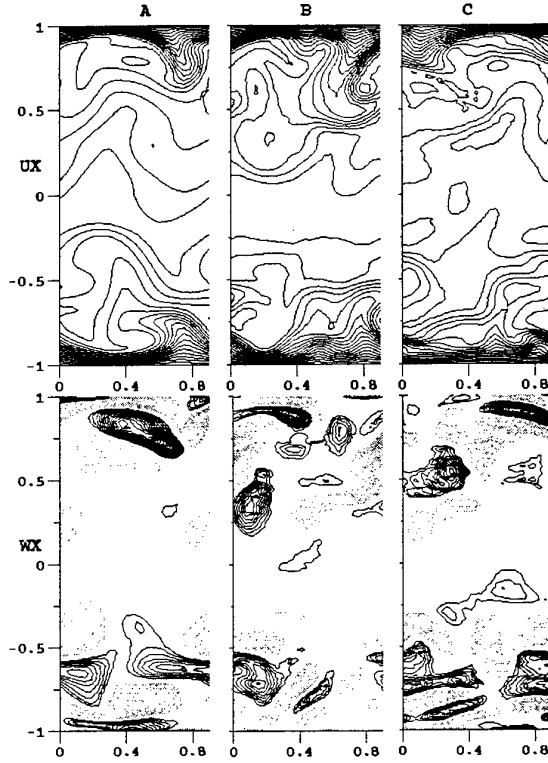

Fig 6. Instantaneous streamwise and spanwise velocity contours in (y,z) plane.

2.5. Driving pressure gradient

In LES of channel flow, it is often felt more natural to conserve the flowrate by driving the flow by means of a mean pressure gradient, rather than artificially rescaling the instantaneous inlet velocities. The mass flux is here sustained by a mean pressure gradient F_1. At each time step, F_1 is function of the variation of mass flux (13):

$$F_1^{n+1} = F_1^n + \rho \frac{\left(Q^n - Q_{ref}\right) - \frac{1}{2}\left(Q^{n-1} - Q_{ref}\right)}{\Delta t\, L_z\, h} \quad \text{with} \quad Q \text{ the}$$

flux, Q_{ref} the imposed flux and L_z the length of the computational box in the homogenous direction.

Fig.7 shows the time history of this external force. For scheme A, the balance between pressure gradient and friction exists. The centred scheme enhances the treatment of the non-linear term and breaks up this equilibrium. By improving the pressure resolution, scheme C recovers this balance. As seen before on Taylor-Green vortices, an identical resolution of velocity and pressure catches the energy exchanges. For the minimal "flow unit", the mean pressure gradient is linked to the mass flux: the poor behaviour of scheme B is attributed to the weak mass conservativity of the P1-isoP2 element in the LES context.

In the frame of RANSE, the velocity - pressure gradient correlation drives the energy exchanges between velocity component. This term is here evaluated from the instantaneous fields and is split in two parts:

$$\Pi_{11} = -\frac{1}{\rho}\left\langle \overline{u}'\frac{\partial \overline{p}'}{\partial x}\right\rangle - \frac{2}{\rho}\left\langle \overline{u}' F_1' \delta_{j1}\right\rangle.$$

The perturbation induced by the forcing term $\left\langle \overline{u}' F_1'\right\rangle$ is

compared to: $\left\langle \overline{u}'^2\right\rangle^{\frac{1}{2}}\left\langle F_1'^2\right\rangle^{\frac{1}{2}}$.

For scheme B this term is of the same order as the mean resolved correlation, thus pressure gradient correction used for maintaining the flowrate seems to introduce an unacceptable numerical artefact. For scheme C this ratio is less than 10%.
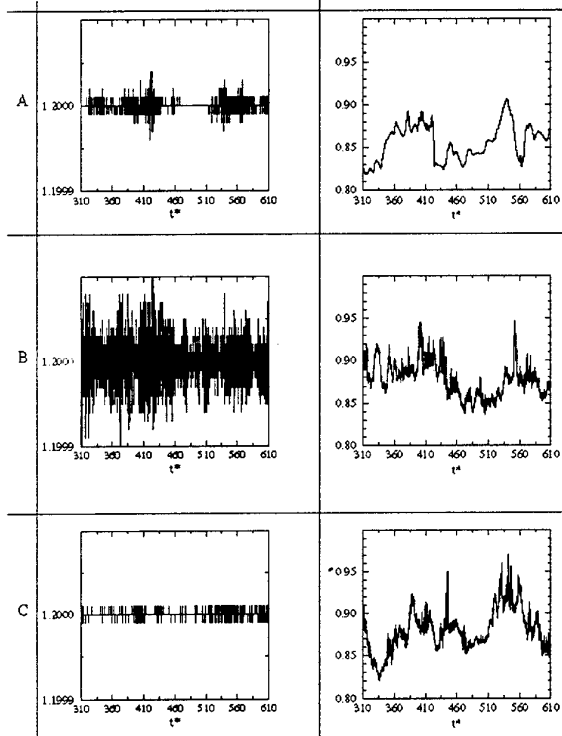

Fig 7: Driving pressure gradient, F_1 (left), and maximum velocity (right) as function of time.

Finally, figure 8 shows the balance of the wall normal fluctuation equation (usually, principally the $\overline{u}^2$ budget is shown since the large magnitude of production masks defects of the other smaller terms). Recovering the dissipation is not expected in this LES, still graph e indicates that with scheme A, small scales are not well resolved, this shows also on the imbalance, graph f. Naturally, under estimation of v' also affects the turbulent transport, graph b.

The final LES version (N3S-LES), has thus deviated significantly from the original code. It is based on a space-&-time-centred, collocated FEM scheme, with linear basis functions on tetrahedral elements. *To conclude, the surprising finding here is that methods which are usually recommended in F.E. textbooks, and* *have indeed been successfully applied to RANSE, are not suitable for LES.*
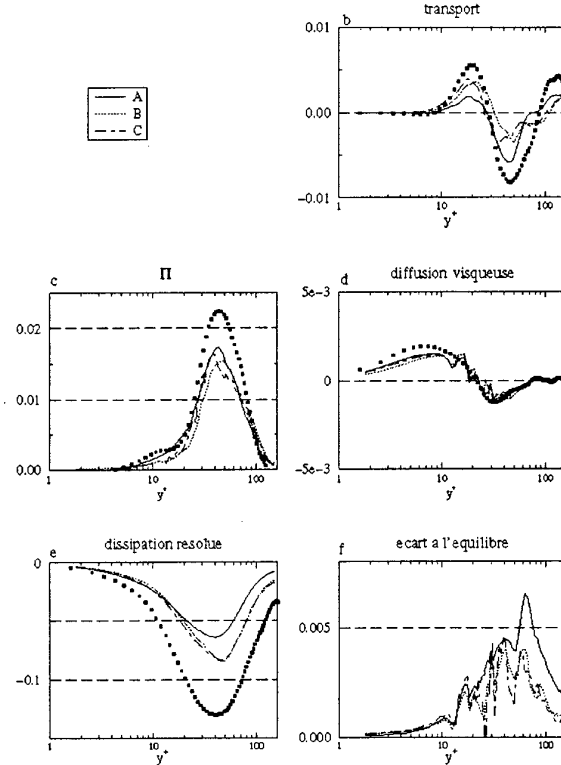

Figure 8 budget of the wall normal Reynolds stress.

3. CROSSFLOW IN TUBE BUNDLE

The flow in a tube bundle is of course of great interest to the power generation industry, not only to study the performance of heat exchangers. Some safety studies involve vibrations through fluid-structure coupling, or large scale temperature fluctuations eventually leading to thermal stripping. The geometry is simple, yet the flow experiences complex strains, making this an attractive test case.
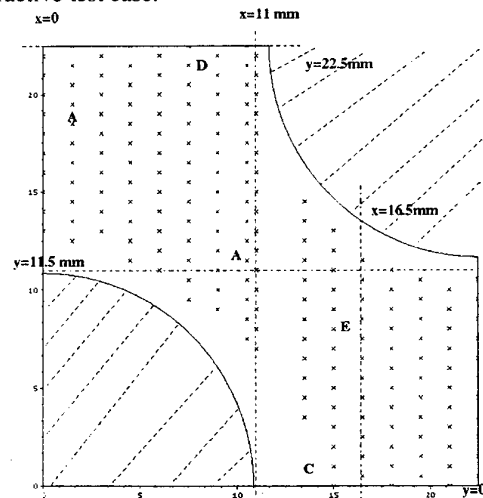

Figure 9 Sub-channel in the tube bundle experiment of Simonin et al. Crosses indicate measurement locations.

3.1. A challenge for RANSE simulations

This flow was considered for the ERCOFTAC/IAHR Workshop on Turbulence Modelling held at UMIST, June 15-16, 1993. The experiment of Simonin & Barcouda (14) provided a database of mean velocities and Reynolds stresses for the flow through an staggered array of tubes. The tube diameters are D=21.7 mm, and the distance between in-line cylinders is L=45.mm. The Reynolds number based on the bulk velocity in the subchannel in between tubes, and tube diameter is 40000.

A variety of models (low Re k-e models, Reynolds Stress Transport, both « standard » and « Realisible » were applied (appendix). Some of the conclusions, as presented by K. Hanjalic & M. Leschziner (15) are the following :

-« Velocity profiles are predicted generally reasonably well, but stress profiles are poor, *particularly in the impinging region* »

-« None of the results show indisputable superiority, though every model refinement and upgrading seems to make a positive contribution »

-« Disappointing : Performances of RSM, though some improvements are discernible (stress behaviour in the impingement region »

The following workshop, Lisbon 94, considered again staggered tube bundles with additional experimental data form Mc Grath, and Kelemenis, but the former provided only near wall data, while some inconsistancy as regards mass conservation were found in the latter. Again performances of RANSE models were disappointing, while interestingly, results using a lattice Boltzman scheme (Eggels) compared fairly well to the near wall data.

Sebag (16) devoted his thesis to the application of standard and elaborate second moment closures to this flow, and concluded that the major improvement in predicting the Reynolds stresses came from a quite simple correction to the dissipation equation (« sensitising dissipation to anisotropy invariant » as proposed by Craft & Launder) and not from the modelling of the pressure strain term at cubic order. Meyer, providing his own experimental database which includes heated tubes also pointed out at the limitations of second moment closures for this tube bundle flow, attributing part of the difficulties to the very high turbulence intensities in this type of flow (35%).

3.2. LES computations

Finally, after the validation of N3S-LES it seemed natural to consider again the experiment of Simonin *et al.*).

The computational domain is sketched on fig. 10. It corresponds to the minimum domain for the instantaneous field without enforcing artificial symmetries. Results will show that no coherent large structure (that might have been generated by periodicity

on a short domain) actually appears. A 2D mesh is generated, structured in the boundary layers, and free (Voronoi) in between cylinders. 33 identical planes are then extrapolated in the z direction, then the prisms are cut into thetahedra, resulting in a total of 405 312 nodes.
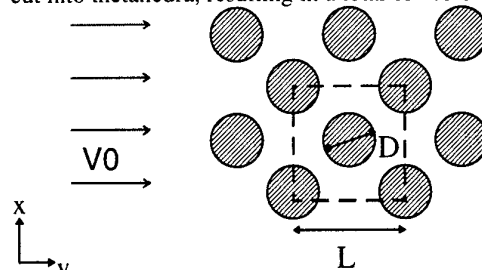
Figure 10 Simonin et al. Exp., Computation subdomain.

The Reynolds number in the LES computation based on bulk velocity in the narrowest section was set to 16 000. With a mean friction velocity of u*= 7 mm/s, the first grid point varies from y+=1.5 to 4 wall units on the circumference of the cylinder. Because local instantaneous values can be significantly higher, wall functions are activated whenever needed. The distortion of the Reynolds number (16 000 instead of 40 000) is expected to have little influence in this flow where the turbulent intensity is 35% (in opposition to flow around a single cylinder).
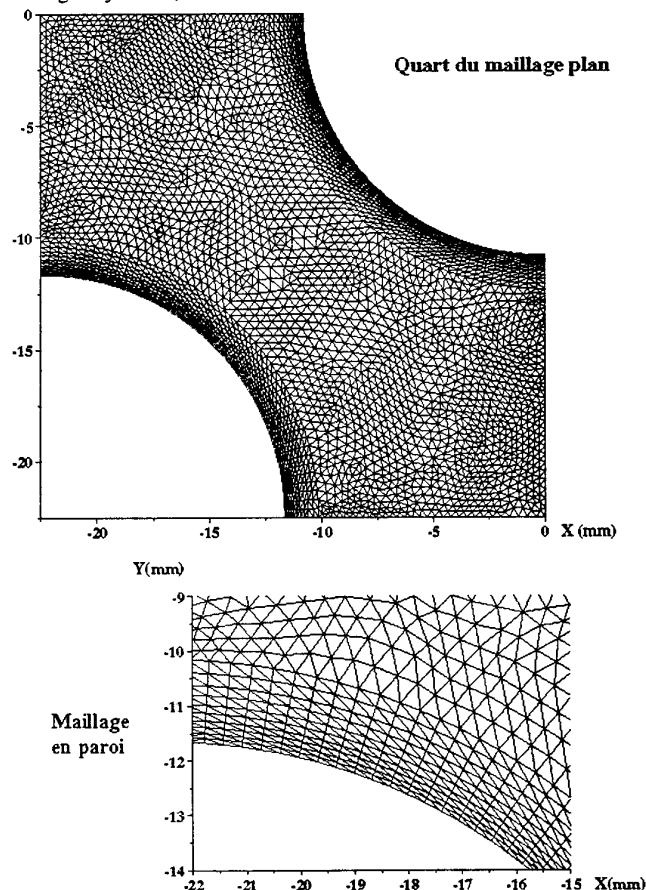
Figure 11 View of 1/4th of a 2D section of the mesh.

A first run was computed with the Smagorinsky model (MS simulation) and, after initialisation, statistics were accumulated over 1.745s, i.e. three domain flow-through (this was found sufficient since spanwise averaging and symmetries are used while gathering statistics). For the second run, with the localised dynamic procedure of Piomelli and Liu (16), statistics were computed over 5 domain flow-through times (3.468 s).

The value of the Smagorinsky constant was set to Cs= 0.065, the dynamic model later yielded somewhat higher values of this coefficient on average, with of course great spatial variability: high values in the separated shear layer, and slightly negative values very near the wall on the upstream half of the tube.
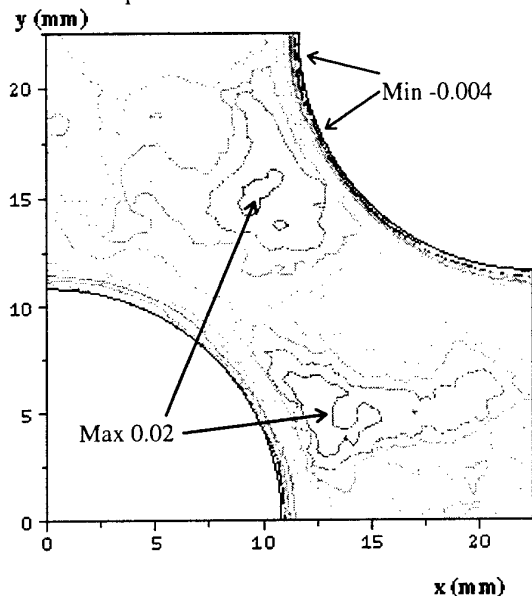

Figure 12, Iso-contours of the SGS viscosity obtained with the dynamic model.

3.3. Statistical results

For the mean velocity, the agreement of the LES with all available data is excellent, and the results from both subgrid-scale models cannot be distinguished. As concerns the Reynolds stresses, the agreement is also good, so we concentrated on the two section for which discrepancies concerning RANSE models were most amplified. Figure 13 shows the wake to impingement axis and the cross section just behind the tube. The striking and unusual feature on the wake axis is that the transverse velocity fluctuation is far larger than the axial one. Thus we approach the stagnation point with

$\overline{u^2} < \overline{v^2}$, and since $\dfrac{\partial \overline{U}}{\partial x} < 0$, the productions of the

stresses and kinetic energy are :

$$P_{uu} = -2\overline{u^2}\frac{\partial \overline{U}}{\partial x} > 0; \quad P_{vv} = +2\overline{v^2}\frac{\partial \overline{U}}{\partial x} < 0$$

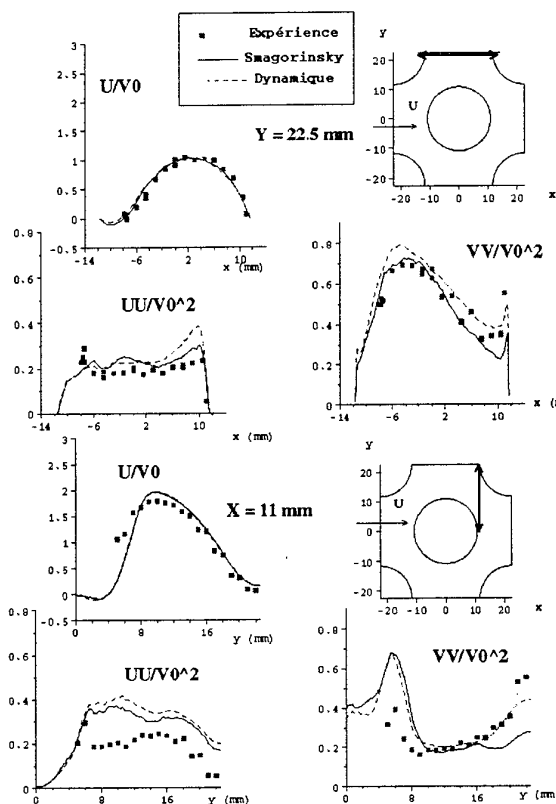$$P_k = -(\overline{u^2} - \overline{v^2})\frac{\partial \overline{U}}{\partial x} < 0$$

Figure 13 First and second moments, solid lines-LES with Smagorinsky model, dashed lines-LES with dynamic model., symbols-experiment (see fig 9)

We notice from the experiment and LES that indeed $\overline{u^2}$ is fairly constant (production balancing dissipation) while $\overline{v^2}$ is decreasing rapidly under the added effects of dissipation and negative production. Since $\overline{u^2} < \overline{v^2}$, even the kinetic energy is decreasing, in opposition to what is found on a stagnation point of a single bluff body, or an impinging jet. Very near the stagnation point, the cinematic blockage of the wall forces $\overline{u^2}$ fluctuation to be converted into $\overline{v^2}$ (« wall echo effect », and the Dynamic model seems to better capture the peak in $\overline{v^2}$, though shown only by one experimental point.
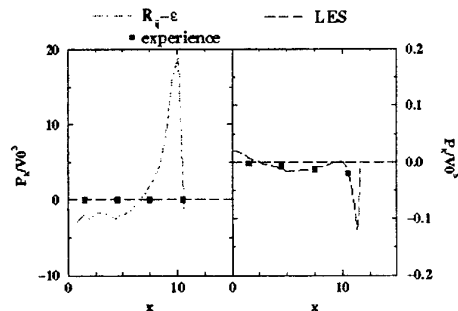

Figure 14 production on the stagnation point axis.

The sharp rise in $\overline{v^2}$ results in a sharp dip in P_k. Figure 14 shows the dramatic overestimation of production given by the second moment closure (note the different scaling). The experiment shows slightly negative values, but data is not available very close to the wall to confirm the sharp dip in P_k shown by the LES.

In the cross section just after the tube (Fig. 13, bottom) at X=11 mm, the first peak in $\overline{v^2}$ is due to the detaching shear layer. The second peak corresponds to the stagnation point, and now there are sufficient experimental points to confirm that the trend given by the dynamic model is more accurate than that of the Smagorinsky model. On figure 12 we had noted that the main difference between the Smagorinsky and Dynamic model is that the latter predicts zero, if not negative, eddy viscosity on the near wall front portion of the cylinder. Vanishing SGS dissipation allows the build up of $\overline{v^2}$. On the other hand, both models overestimate $\overline{u^2}$. Since the turbulent viscosity is equal to five times the fluid viscosity in most regions, some effect of the subgrid-scale model was expected, but in any extent, this is much smaller than the extreme variability observed in the aforementioned workshops on RANSE models. From figure 13, it cannot be conclude from the mean velocity U, that the recirculation bubble is accurately predicted (for lack of data). But further downstream, at X= 16.5 mm (figure 15) we again see excellent agreement with the experimental data for both models on the U and V components. Notice also the very large values of the w' fluctuations compared to u' and v' , especially on the boundary of the upper cylinder.

Figure 15 (see fig. 13)

3.4. Instantaneous velocity fields

Visualizations of instantaneous iso-streamwise velocities (left) show that large structures of low velocity (in blue/light grey, in circle) are detached from the wake and transported towards the stagnation point (flow is from left to right). High velocity blobs (red/dark grey, in ellipse) occasionally make incursions in this region. An explanation for the difficulties of standard RANSE models may be that in this wake-to gap region, the fluctuating velocities are larger than the mean. It is thus difficult to reconstruct the flow characteristics, from the sole mean velocity. In particular, the so called « wall echo effect » introduced in second moment closures were devised to represent the « splatting » of small eddies against an infinite (compared to the integral scale) plane wall. In the present case, as seen form the instantaneous fields, the size of the structures is comparable to the cylinder size. For instance the eddies are large enough to « feel » the curvature of the wall, i.e. at the stagnation point one could imagine that the wall normal fluctuations are more easily transferred into lateral fluctuations because of this strong curvature.

Finally, we have pointed out the relatively large velocity fluctuations in the homogeneity direction.
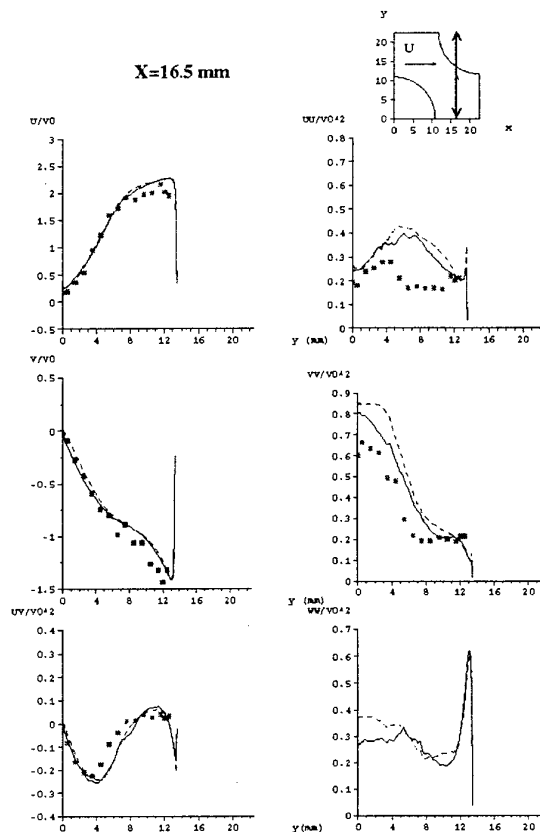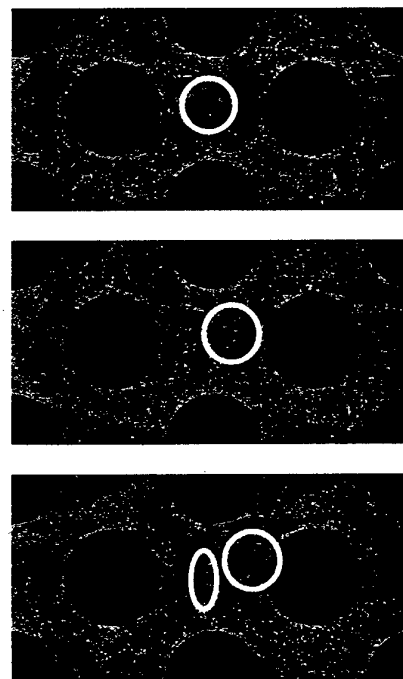

Time sequence of instantaneous iso-streamwise velocities.

Particles emitted from a vertical line (bottom left) are spread out in the whole spanwise dimension, showing the fully three-dimensional nature of the flow. This flow is probably an ideal case for the modelling the mysterious « wall echo » terms. Indeed they play here a dominant role, since overall, the w' fluctuations (for which there is no direct production) are significantly larger than the streamwise fluctuations which are alternatively generated by shear and damped by cinematic blocking.
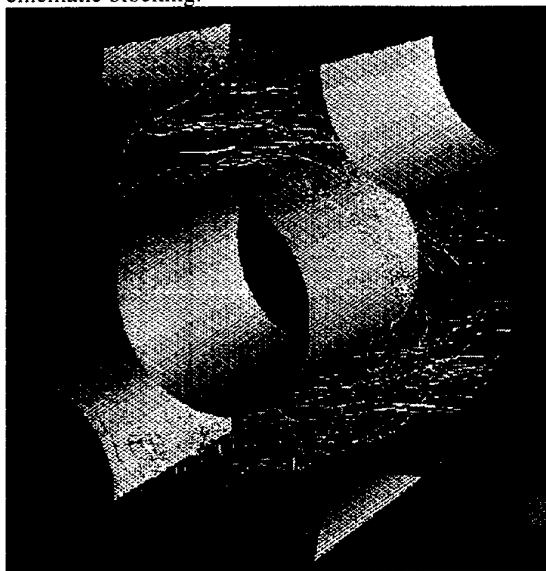
4. CONCLUSIONS AND PERSPECTIVES

It has been shown that a standard « industrial » code cannot be straightforwardly used for LES which requires specific dicretizations. The low-order FE scheme was tested on turbulent flows. This analysis underlines that the "safest" element is not adapted to LES: this statement was suggested by the literature on Finite Element[11,18], but the limitations appear clearly on LES of turbulent flows.

The simulation of the flow in a tube as a first application of LES in complex geometry yielded excellent agreement with experimental data, whereas previous RANSE simulations had failed. This is not « beginner's luck », LES was successful because the size of the larger eddies are of similar order as that of the obstacles, whereas RANSE models encounter limitations precisely when the integral length-scale of the turbulence is comparable with that of the mean flow inhomogeneity (this interpretation was previously proposed concerning the effect of the Reynolds number on the recirculation behind a step (19)). Thus it may seem that to much effort has been devoted to academic flows, e. g . channel flows, where RANSE models yield excellent results for tremendously less efforts. Thus there seems to be a complementary potential between LES and RANSE and they should not be in considered in competition (just as there is no point in insisting on using the full 3D Navier Stokes equations for coastal engineering applications instead of the shallow water equations (on France's shallow coasts). Similarly, LES of the boundary layer of an airfoil at low incidence will remain out of reach for very long (if not pointless), given the smallness of the turbulent structures compared to the airfoil, and given the reliability of RANSE models for such flows. On the other hand small bluff bodies, e.g. electronic components in a highly turbulent channel flow, as considered in the 1997 ERCOFTAC/AIHR workshop does seem an LES application.

The follow up of the present simulation was logically heat transfer, but a new project, in collaboration with the French atomic energy commission (CEA) has just started with the objective of developing an LES code for unstructured meshes for massively parallel computers (T3E). The aim is to perform LES of complex geometries with over 10 million nodes, and the tube bundle test case will be considered again, hopefully providing this time a complete database (due begining of 1998) of the budgets of the second moment closures, including heat transfer.

References

1. M. Breuer and M. Pourquie 1996 "First Experiences with LES of flows past Bluff Bodies" *Eng. Turbulence Modelling and Exp.*, 3:177-186

2. K. Jansen 1993 "Unstructured grid large eddy simulation of wall bounded flows" *Ann. Res. Briefs CTR*

3. DucrosF., Nicoud F., Shonfeld T. 1997 « LES of compressible flows on hybrid meshes », *Turbulent Shear Flow 11, Grenoble, France.*

4. P. Rollet-Miet 1997 "Simulation des Grandes Echelles sur maillages non structurés pour géométries complexes" *PhD Thesis Ecole Centrale de Lyon*

5. J.P. Chabard, B. Métivet *et al.* 1992 "An efficient finite element method for the computation of 3D turbulent incompressible flows" *Finite Elements in Fluids*, Vol. 8

6. Laurence D., 1998, « Advective Formulation of LES », in Direct and Large Eddy Simulation of Turbulence, EUROMECH col. N 199, Munich 1985 (Schuman, Friedrich Eds.)

7. M. Oshima, T. Kobayashi *et al.* 1996 "Development of filtering operation for dynamic SGS model using finite element method" *2d Ercoftac Workshop on Direct and Large Eddy Simulation* Grenoble

8. M. Bercovier and O.A. Pironneau 1977 "Error estimates for finite element method solution of the Stokes problem in the primitive variables" *Numer. Math.* 33:211-224

9. F. Brezzi and M. Fortin 1991 *"Mixed and hybrid finite elements"* Springer

10 D. Pelletier, A. Fortin and R. Camarero 1989 "Are FEM solutions of incompressible flows really incompressible?" *Int. J. for Num. Meth. in Fluids* 9:99-112

11. J. Jimenez and P. Moin 1991 "The minimal flow unit in near-wall turbulence" *JFM* 225: 213-240

12. R. Boudjemadi 1996 "Simulation numérique directe et modélisation de la convection naturelle turbulente dans un canal différentiellement chauffé" *Ph.D. Thesis Paris VI*

13. V. Deschamps 1988 "Simulation numérique de la turbulence inhomogène incompressible dans un écoulement de canal plan" *Ph.D. Thesis INPT*

14. O. Simonin, M. Barcouda 1988 "Measurements and prediction of turbulent flow entering a staggered tube bundle" *Fourth Int. Symp. on App. of Laser Anemometry to fluid mechanics* Lisbon, Portugal

15. Hanjalic K., Leschziner M., 1993, Report-Back on ERCOFTAC/IAHR Turbulence Modelling Workshop held at Umist, June 15-16, 1993.

16. U. Piomelli, J. Liu 1994 "Large eddy simulation of rotating channel flows using a localised dynamic model » *Phys Fluids* A7

17. S. Sebag, V. Maupu, D. Laurence "Non-orthogonal calculation procedures using second moment closure" *TSF* 8

18. T.J.R Hughes 1987 *The Finite Element method* Prentice-Hall.

19 Laurence D., Parneix S. « Second Moment Closure analysis of a DNS backstep flow database », 1997, Turbulent Heat and Mass Transfer 2, Delft University Press (Hanjalic, Peeters Eds.)

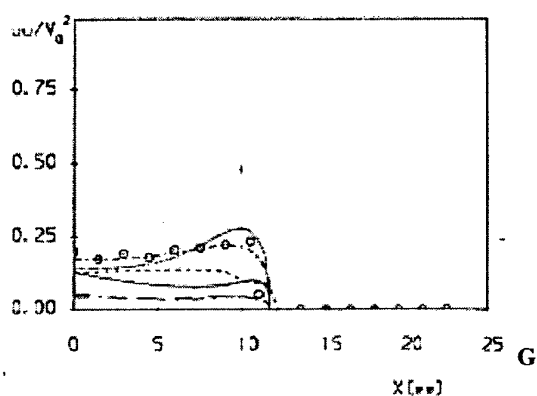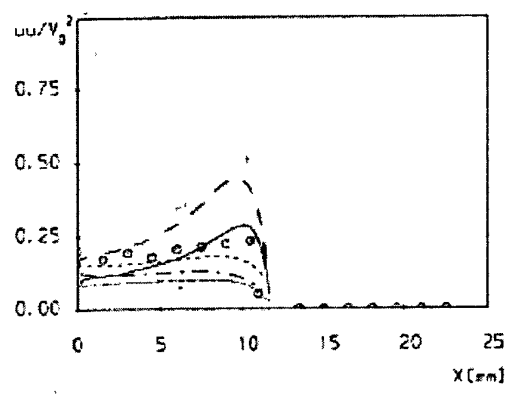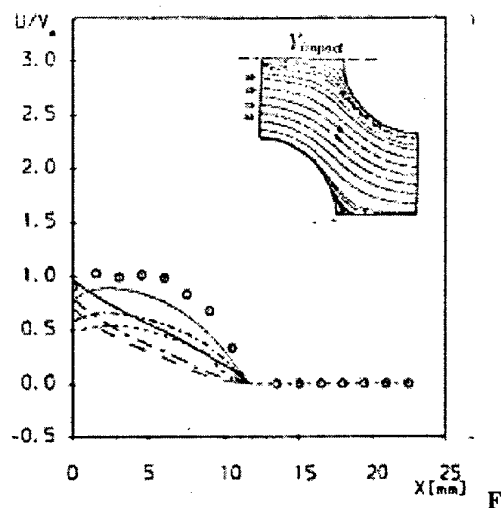**Appendix : RANSE 1993 Workshop Results (15)**
(all graphs by T. Craft)

A

B

C
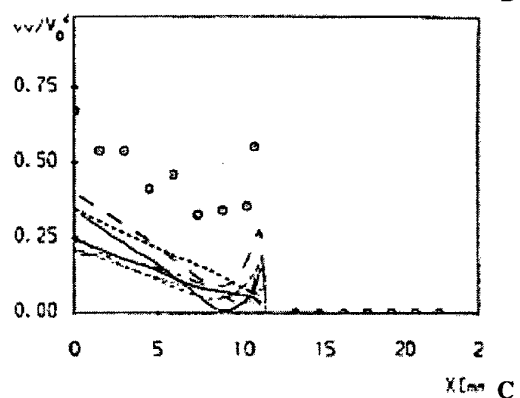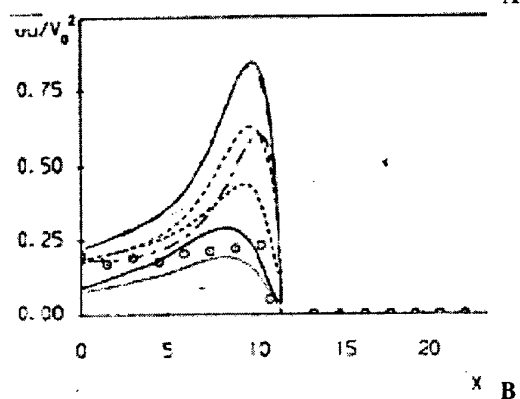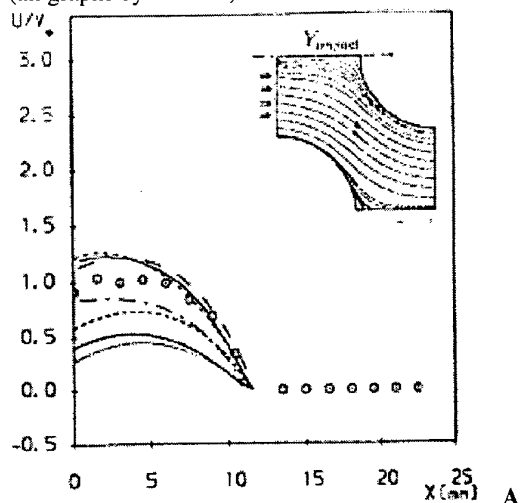
A,B,C : Various Low-Re 2 equation models
The 3 sets of data (UMIST) corresponding best to the exp ; for the mean velocity (A) correspondingly give the highest turbulent kinetic energy levels.
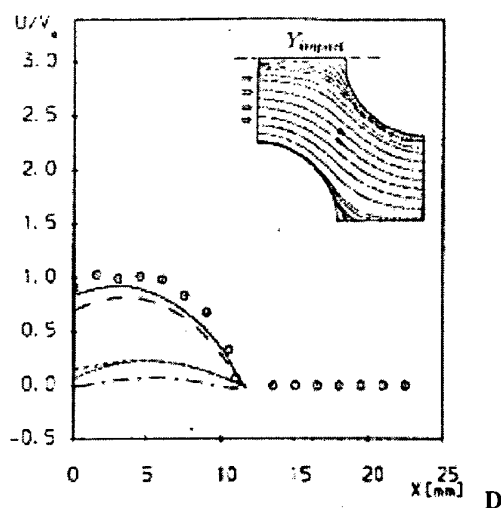
D-E : RNG models. Models were checked to be identical, the large differences observed are attributed to a bifurcation : as the kinetic energy level is reduced by the RNG correction, the flow is allowed to stagnated in between tubes, with little mixing from the principle flow passing the tubes with a minimum meandering effect. Less mean flow deformation in turn yields less turbulence production.

F, G, H : Second moment Closures
Standard IP model seems to yield « best » results

yet $\overline{v^2}$ is severely underestimated
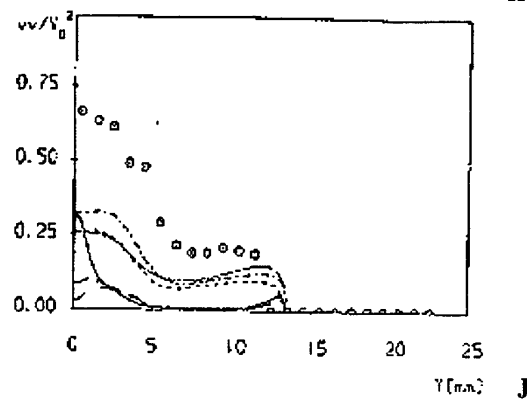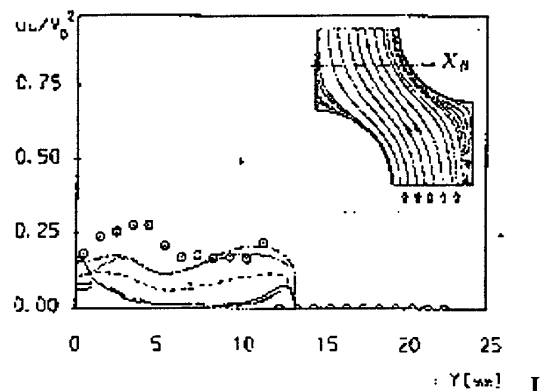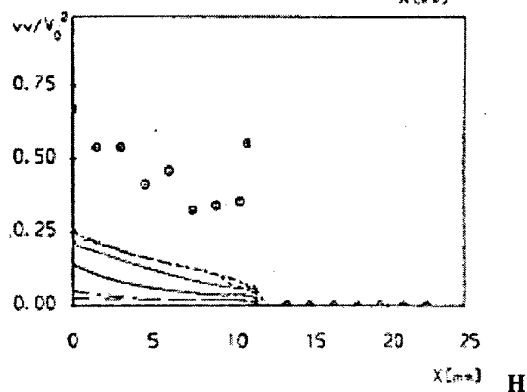
I, J : cross-section after the tube (cf. fig. 15)

$\overline{v^2}$ is still severely underestimated in the wake.

TURBULENT HEAT TRANSFER MEASUREMENTS USING LIQUID CRYSTALS

P. T. Ireland, A. J. Neely, D. R. H. Gillespie and A. J. Robertson

Department of Engineering Science, University of Oxford,
Parks Road, Oxford. OX1 3PJ

ABSTRACT

The transient method of measuring heat transfer coefficients that uses liquid crystals, since its beginnings in the early 1980s, has become one of the best ways of determining full surface distributions of heat transfer coefficient. The turbomachinery research group at Oxford has concentrated on the application of the method to numerous mechanical engineering thermal problems specific to the jet engine. The paper summarises some of the recent developments in the technique including the implementation of an elegant way of producing a change in the fluid temperature. Recent, high-density heat transfer coefficient measurements are discussed and a means of integrating the measurements into finite element software for subsequent data analysis is presented. The paper should be of interest to engineers interested in using the most modern heat transfer measurement techniques in their research and development programmes.

1. BACKGROUND

The transient method of measuring heat transfer to thermally insulating models of mechanical engineering components has become established as one of the most effective ways of measuring complete distributions of local heat transfer coefficient. Its advantages include the provision of data over the complete surface in one experiment; its high accuracy and the ease of model manufacture. The accuracy depends on both the experimental conditions and the sophistication of the image processing applied to the liquid crystal colour play. In its most straightforward implementation, the uncertainty in heat transfer coefficient is on the order of 6%, see Baughn et al. (2), though image processing that uses the full time content of the video data can improve this. When local heat transfer coefficients processed in an image are referenced to an accurately known heat transfer coefficient, the accuracy in heat transfer coefficient ratio can be very high (on the order of 2%)- see Wang et al.(22).

The models are made from a good thermal insulator, normally perspex, and only require the application of a limited number of surface thermocouples for crystal calibration and determination of the initial temperature. This makes the method particularly suitable to the measurement of heat transfer coefficients on complex shaped surfaces. Chyu et al. (3) used the method to measure the heat transfer coefficient to dimples used to promote heat transfer in internal cooling passages. Wang et al. (21) investigated the heat transfer coefficient distribution over an isolated pedestal (or pin fin) with fillet radii. Recent examples of the technique applied to external heat transfer coefficients include Robertson et al. (14) and (15).

2. ESTABLISHMENT OF THE THERMAL TRANSIENT

2.1 Mesh heater concept

Numerous strategies have been used to establish the temperature difference between the fluid and model surface. Early experimental arrangements included electrical heaters that took time to stabilise at the required temperature, (4). The heat transfer measuring method is better conditioned if the fluid temperature undergoes a sudden change at the start of the test. For this reason, the heater time constant was overcome by using plumbing which allowed the flow to by-pass the test section whilst the former heated up. Fast acting valves were then switched to start the heat transfer experiment. Other approaches include rapidly inserting a pre-heated or pre-cooled model into the wind tunnel. The large-scale annular cascade facility at Oxford uses a pair of shutters to isolate the instrumented section of the annulus from the substantial flow, Martinez-Botas et al. (8). Figure 1, that spans the fluid supply duct, Gillespie et al (6).

2.2 Applications

The system has been used for research into turbine blade cooling systems, (5) and (20), for investigating extended heat transfer surfaces for cooling engine components and for film cooling experiments (1). The largest mesh heater, Figure 2, to date consumes more than 40kW and is used to heat a high flow rate tunnel (~10m^3/s) at speeds ranging from 5 to

30m/s. This work has been reported in Neely et al. (11) and led to the optimisation of extended surface shapes used to cool the outside of engine components- see Robertson et al (14). In this case, the electrical power consumption was reduced by supplying current to only the central section of the duct. The powered section was then surrounded by two un-powered meshes and analysis was performed to ensure that the unheated flow did not encroach on the centrally positioned heat transfer model. A small (~1mm) gap prevented current passing from the central to the surrounding meshes. Figure 3 shows the velocity measured 340mm downstream of the mesh and clearly shows the small jet caused by the gap between the unheated and the heated meshes. The affect on the flow temperature can be seen in Figure 4 where the unheated and heated zones are clearly denoted. The small jet temperature will be between that of the heated and unheated zones and does not show up clearly in this figure.

Careful engineering of the mesh carrier ensures that the temperature of the wires is uniform so that a uniform flow temperature is achieved downstream. An image representing the mesh temperature is included as Figure 6. The mesh temperature is uniform to within 1.3°C in this case where the flow temperature is being increased by 20°C. The mesh convective efficiency, defined as

$$\eta = \frac{T_{downstream} - T_{upstream}}{T_{wire} - T_{upstream}}$$

depends on the air speed, but in this case (at 5m/s) η is approximately 0.55. The non-uniformity in downstream temperature can be calculated as 3.5% of the temperature increase.

The most recent meshes have been used to heat moderately high pressure (~100psi) air for further impingement research, Figure 7. For a fixed mass flow rate, heating the air at higher upstream density is an effective means of reducing the mesh face velocity (for fixed area) and this allows the heater size to be reduced. The heater mesh in the figure is being used to rapidly switch the flow temperature in a programme of impingement cooling research.

2.3 Mesh heater advantages
The mesh used has a through flow to projected area quotient of 0.38 and can, under correct lighting conditions, be transluscent. Figure 8 shows an arrangement used to measure heat transfer coefficients to engine components where the flow is from a large nozzle through a polycarbonate perforated plate(10). Figure 9 shows an image of the liquid crystal coated perspex model taken from a miniature camera position inside the nozzle assembly. The camera looks through the mesh and the use of a wide camera aperture effectively removes the mesh from the image. The calculated heat transfer coefficient distribution is presented in Figure 10. The same approach has been used by Gillespie et al. (6) to measure the heat transfer coefficients on the upstream surface of an impingement plate, Figure 11.

All of the electrical power supplied to the mesh heats the air so that an accurate measurement of the average temperature increase can readily be achieved by measuring the power supplied to the mesh.

$$T_{downstream} - T_{upstream} = \frac{IV}{mc_p}$$

This approach has proved very useful in low speed flow situations where the time response of the gas measuring thermocouple is prohibitively slow. Figure 12 shows the level of agreement between the calculated and measured temperatures for recent blade cooling passage experiments, Tsang and Ireland (18).

In some situations it may be desirable to generate a temperature profile using unheated, heated combinations of the mesh in series. This could allow profiles that have an artificially thick cool region near the wall to be produced.

Heat transfer measurements in impingement systems are difficult for a number of reasons. The local heat transfer coefficient changes by a large factor from a peak at the stagnation point beneath the jet to significantly lower values away from the jet in the channel between impingement and target plate. One difficulty specific to the transient method is the problem of quickly establishing the flow at a temperature different to the starting temperature. In a typical impingement array, the area ratio between the plenum feeding the jets and the total cross-sectional area of the jets means that the flow velocity in the plenum is very low. This is the region in which flow switching needs to be performed and this leads to problems. Van Treuren et al. (19) used a complicated by-pass system that passed heated air into the plenum for 30minutes prior to the start of the transient experiment. The test section was prevented from pre-heating by bleeding room temperature air through the model into the

2

plenum. Three electrically operated fast acting valves were synchronised to initiate the transient heat transfer experiment. The flow temperature switching in later impingement heat transfer experiments is now achieved using a planar heater mesh fitted across the plenum flow. The apparatus no-longer requires any fast acting valves since the experiments start when power is switched to the mesh. Prior to this stage, room temperature air is drawn through the heater mesh and model.

The velocity through the heater mesh in impingement experiments is typically low and a step change in the power supplied does not cause the flow temperature to change as a step. The normal surface temperature response of the perspex substrate under a step change in fluid temperature is given by the familiar equation

$$T_s = T_0 + \left(T_g - T_0\right)\exp(\frac{h^2 t}{\rho c k})$$

$$\times erfc(\frac{h\sqrt{t}}{\sqrt{\rho c k}})$$

When the heat transfer driving fluid temperature changes with a time constant, τ, the equation for the surface temperature rise becomes, (6),

$$\frac{T}{T_g} = 1 - \frac{\frac{\rho c k}{h^2 \tau}}{\left(1 + \frac{\rho c k}{h^2 \tau}\right)} e^{\frac{h^2 t}{\rho c k}}$$

$$erfc\left(\frac{h\sqrt{t}}{\sqrt{\rho c k}}\right) - e^{-\frac{t}{\tau}}\frac{1}{\left(1 + \frac{\rho c k}{h^2 \tau}\right)}$$

$$\left(1 + \frac{\sqrt{\rho c k}}{h\sqrt{\tau}}\left(\frac{\frac{1}{\pi}\sqrt{\frac{t}{\tau}} + \frac{2}{\pi}\sum_{1}^{\infty}\frac{1}{n}e^{-\frac{n^2}{4}}}{\sinh n \sqrt{\frac{t}{\tau}}}\right)\right)$$

The above equation is then solved numerically for the local heat transfer coefficients from the time, t, the surface takes to reach the known liquid crystal temperature.

In situations when the gas temperature change is neither a step change nor a first order lag, the fluid temperature should be measured and the measured signal used in a numerical procedure that sums the surface response to multiple delayed steps, Metzger and Larson (9) or multiple delayed ramps, Saabas et al. (16).

3. APPLICATION TO IMPINGEMENT COOLING RESEARCH.

Progress in the hardware used at Oxford has centred around a change in the frame grabbing strategy. The card that digitises the video recording is fitted to a Pentium PC and the ditized data stored directly in computer RAM. The computer has 195Mbytes of ram fitted and is capable of acquiring 62 full frames. In practice, not all pixel information is required to resolve accurately typical heat transfer coefficient results. In addition, not every frame is required for heat transfer processing. A typical heat transfer test lasts several seconds and the data is digitised over two or three sweeps. Each frame is captured at a particular time from the start of the heat transfer experiment. A time signal is captured in the frame and used to reference the intensity signal to the elapsed time.

4. IMAGE PROCESSING- HIGH RESOLUTION HTC DATA

Figure 13 shows the heat transfer coefficient distribution on the target plate beneath an array of impinging jets. The work is notable for the high data resolution that shows how repeatable the heat transfer coefficient signature between rows. The exit from the channel is from one side and spent flow from the early rows forms a cross-flow on the later jets. The research is reported further in (12) and (17).

The image processing strategy here was to use a combination of three different narrow band liquid crystals that produce peaks in intensity at three calibrated temperatures at every pixel. Each image includes more than 5000 points and the high data resolution can be seen to reveal interesting features about the flow field. The repeatability of the bump in heat transfer beneath each jet is very noticeable even though each jet is subjected to a differing amount of cross-flow. In this arrangement, three different hole sizes have been used. The first three rows of holes have the same diameter. The fourth and fifth rows have larger diameter holes. The last row has an even larger diameter. One feature that seems repeatable is the change in heat transfer coefficient slope that exists between 1.1 and1.5d from the hole axis.

Earlier liquid crystal experiments at Oxford by van Treuren tested an array with a bigger spacing between holes. His data, at a slightly lower resolution, exhibited the same shaped bumps beneath the jets. Figure 14 shows present data normalised by the stagnation point heat transfer coefficient. The results from van Treuren have also been included and, despite a

hole spacing to diameter ratio more than twice the present value, there is remarkable similarity between the heat transfer coefficient variation. Van Treuren's measurements were made in a transient heat transfer facility in which the impingement plate was water cooled to maintain a constant temperature. The liquid crystal data were processed to obtain both the heat transfer coefficient and the adiabatic wall temperature. The latter was then expressed as a dimensionless temperature difference ratio. The present data were from a fully perspex rig in which the impingement plate was allowed to warm up during the experiment. The heat transfer driving temperature is then the temperature downstream of the heater mesh (the plenum temperature) as can be seen from the heat flux- temperature plot included as Figure 15. The data here could be applied to systems in which the plate temperature is the same as the plenum temperature.

5. DATA RECOVERY FROM LIQUID CRYSTAL EXPERIMENTS.

The subject of automatically recovering the liquid crystal colour change times from video recordings of experiments has been addressed by Robertson, (13). The software links the co-ordinates of a numerically defined model into pixel co-ordinates using an analytic model of the optical system. When linked to the heat-transfer-solving program, the software can automatically extract the measured heat transfer coefficients in real co-ordinates. This has proved invaluable for finite element analyses of real engine components where the actual temperature is influenced by lateral conduction occurring in a metallic component.

6. CONCLUSIONS

The paper summaries recent progress in what has become an established method of measuring distributions of local heat transfer coefficient. Since its introduction three years ago, the mesh heater has rapidly replaced other heaters as a very convenient (and hence low cost) way of producing the thermal transient. The paper describes the mesh and gives several recent applications of its use. The translucent nature of the mesh has allowed camera views through the heater and examples are given of the use of this advantage. The uniformity of the mesh has been discussed and a means of reducing the total electrical power by including un-powered sections presented. The mesh has been shown to be suitable for heating atmospheric and super-atmospheric flow. The mesh has been used to research the one of the most difficult cooling systems- that of impingement cooling. In this situation, the

change in driving temperature is achieved easily and the needed for complicated plumbing to pre-heat the plenum avoided. Progress in the image processing has increased the data point resolution. A very exciting computational method for determining the co-ordinates of model surface at which the crystal changes colour has been introduced.

7. ACKNOWLEDGEMENTS

8. NOMENCLATURE

|	
c_p	specific heat at constant pressure for air, J/kgK
c	specific heat of perspex, J/kgK
h	heat transfer coefficient, W/m²K
I	current, Amps
k	thermal conductivity of perspex, W/mK
m	mass flow rate, kg/s
t	time, s
T	temperature, °C
V	voltage, V

Greek

η	mesh convective efficiency
ρ	density, kg/m³
τ	time constant, s

Subscripts

|	
g	gas
O	starting
s	surface

9. REFERENCES

(1) Allen, C, " A computational and experimental examination of film cooling ," D.Phil thesis, University of Oxford, 1996.
(2) Baughn, J.W., Ireland, P.T. and Jones, T.V.," A Comparison of the Transient and Heated-coating Methods for the Measurement of Local Heat Transfer Coefficients," *ASME paper, 88-GT-180* and later in the Journal of Turbomachinery, 1988.
(3) Chyu, M.K., Yu, Y., Ding, H., Downs, J.P. and Soechting, F.O.,"Concavity enhanced heat transfer in an internal cooling passage," ASME paper 97-GT-437.
(4) Clifford, R.J., Jones, T.V and Dunne,S.T.," Techniques for obtaining detailed heat transfer coefficient measurements within gas turbine blade and vane cooling passages, ASME paper 83-GT-58, 1983.

(5) Gillespie, D. R.H., Wang, Z., Ireland, P.T.and Kohler, S.T.," Full surface local heat transfer measurements in a model of an integrally cast impingement cooling geometry,"Journal of Turbomachinery, vol.120, 1998, pp. 92-99.

(6) Gillespie,"Intricate internal cooling systems for gas turbine blading," D.Phil thesis, University of Oxford, 1996.

(7) Gillespie, D. R. H., Wang, Z. and Ireland, P.T,"Heating Element," British Patent Application PCT/GB96/2017, 1995.

(8) Martinez-Botas, R.F., Lock G.D and Jones, T.V.,"Heat transfer measurements in an annular cascade of transonic gas turbine blades using the transient liquid crystal technique," Journal of Turbomachinery, vol. 117, pp.425-431, 1995.

(9) Metzger, D.E. and Larson, D.E.," Use of melting point surface coatings for local convection heat transfer measurements in rectangular channel flows with 90o degree turns," Journal of heat transfer, vol. 108, pp.48-54., 1986.

(10) Neely, A. J., Ireland, P. T. and Mullender, A, "Validation of Novel Low-Temperature Fire Event Modelling Technique", To be presented at the Royal Aeronautical Society conference, Verification of design methods by test and analysis, 23-24th November, 1998.

(11) Neely, A.J. Ireland, P.T. and Harper," Extended surface convective cooling of engine components using the transient liquid crystal technique,"Journal of Power and Energy Vol 211, Part A, pp 273-287, 1997.

(12) Michaelis, M, Robertson, A.J. and Ireland,P.T.,"Detailed heat transfer coefficient measurements in an engine representative impingement cooling system,"OUEL report, 1998.

(13) Robertson, A.J."Extended surface heat transfer performance," D.Phil thesis, University of Oxford, 1998.

(14) Robertson, A. J., Neely, A. J., Ireland P. T. and Harper, L.R.," Local coefficients of heat transfer on optimised finned cylinders "Proceedings of the 36th Aerospace Sciences meeting, Reno, January 12-15, paper AIAA 98-0875. 1998

(15) Robertson, A.J., Neely, A.J. and Ireland, P.T.,"Local heat transfer coefficients on flat continuous, interrupted and corrugated external fins," ASME paper 97-GT-380 presented at I.G.T.I. conference, Orlando,1997

(16) Saabas, H.J, Arora, S.C and Abdel Messeh,"Application of the transient test technique to measure local heat transfer coefficients associated with augmented airfoil cooling passages," ASME paper 87-GT-212, 1987.

(17) Son C M, Michaelis, M., Robertson, A.J. and Ireland, PT., "Detailed heat transfer coefficient measurements in an engine representative impingement cooling system using liquid crystals," submitted to the Int. Mech. Eng. Congress and Expo., Anaheim CA, 1998

(18)Tsang C. and Ireland, P.T., "Temperature variation in a long passage during a transient heat transfer experiment," OUEL report, 1998.

(19) Van Treuren, K. V., Wang, Z., Ireland P.T. and Jones, T.V., " Local heat transfer coefficient and adiabatic wall temperature measurements beneath arrays of staggered and inline impinging jets," ASME paper 94-GT-181.

(20)Wang Z., Ireland P. T., Kohler S. T. and Chew J., "Heat transfer measurements to a gas turbine cooling passage with inclined ribs," Journal of Turbomachinery,.Vol 120, pp 63-69.(Also ASME 96-GT-542), 1998

(21) Wang, Z., Ireland, P.T. and Jones, T.V.," Detailed Heat Transfer Measurements and thermal analysis at engine conditions of a pedestal with fillet radii,"*ASME* Journal of Turbomachinery, vol. 117, pp. 290-297. 1995.

(22) Wang, Z., Ireland, P. T., Jones, T. V., and Davenport, R., 1994," A Colour Image Processing System For Transient Liquid Crystal Heat Transfer Experiments," *ASME* Journal of Turbomachinery, vol. 118, pp. 421-427.
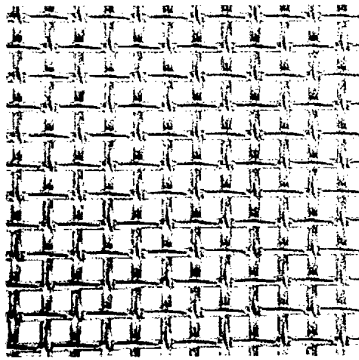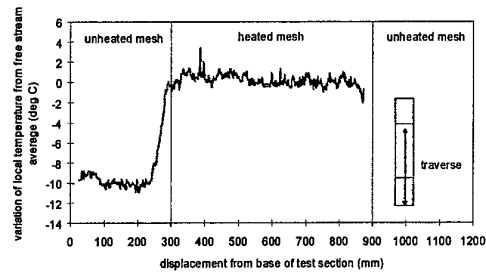
**Figure 1 Close up of heater mesh. Wire diameter is 40μm.**
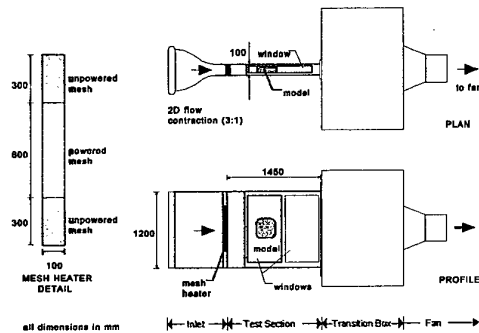
**Figure 2. Heat transfer tunnel used to investigate the thermal performance of extended surfaces.**
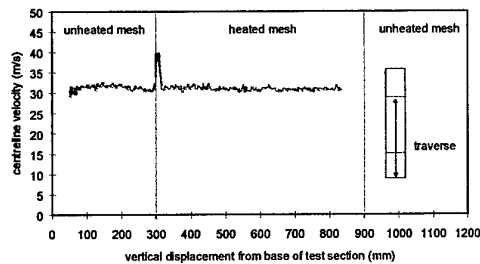
Figure 3 Velocity profile measured 340 mm downstream of the heater mesh showing the edge of the heated and unheated sections.

Figure 4. Vertical temperature traverse measured 370 mm downstream of the heater mesh in extended surface research tunnel
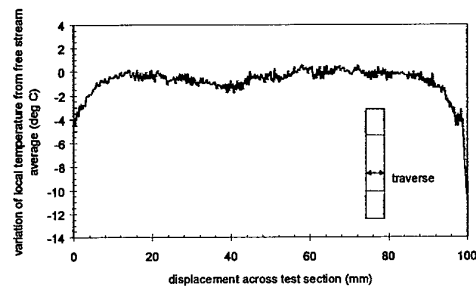
Figure 5. Horizontal temperature traverse measured 370 mm downstream of the heater mesh in extended surface research tunnel (130 mm below the cenreline).
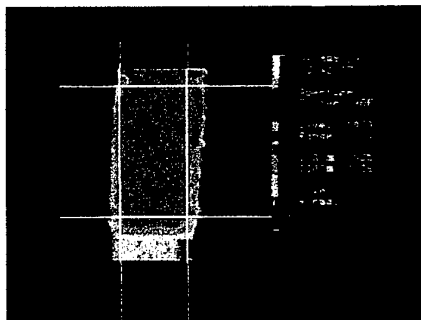
Figure 6 IR image of the heater mesh fitted to the plenum of the rig used to make the heat transfer measurements to the impinging jets. The extent of the mesh is between the white lines and the surounding signals are reflections from the rig intake.
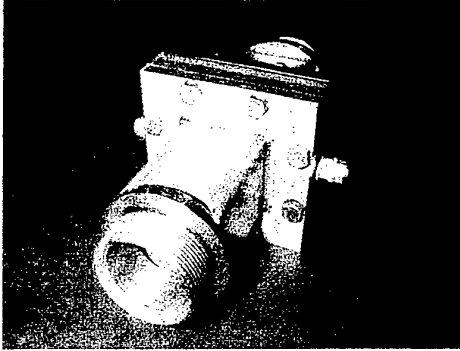
Figure 7 Heater mesh arrangement used to heat high pressure air. Pipe i.d. is 50mm.

Figure 10. HTC distribution (W/M^2/K) deduced from video history of view through the mesh and porous Perspex plate in the fire-test rig

Reynolds Number = 38000   Image at time = 60 seconds
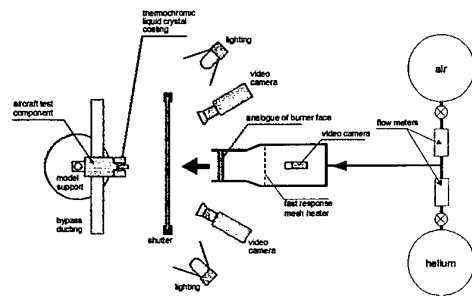

Nusselt Number

Figure 8 Arrangement used to measure heat transfer coefficients to engine components. Flow is from large nozzle including a perforated plate.
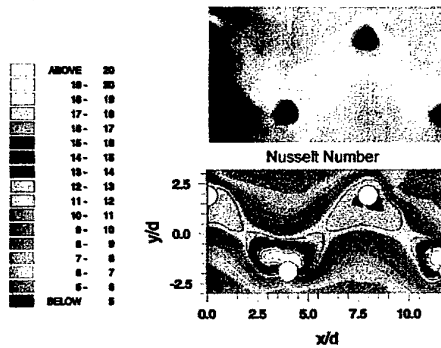
Figure 11 Nusselt number contours on the front face of a plate used to produce impinging jets. The upper image is from a camera viewing through the heater mesh.

Figure 9. Image of engine mount ring through the mesh and porous Perspex plate in fire test rig
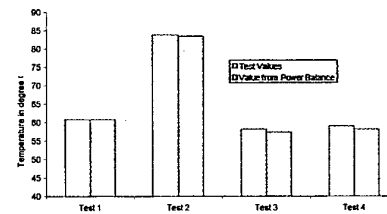
Figure 12 Temperature increase calculated from power supplied versus measured fluid temperature increase for a typical blade cooling experiment. Note the false origin-temperature upstream of the mesh is approximately 20°C.
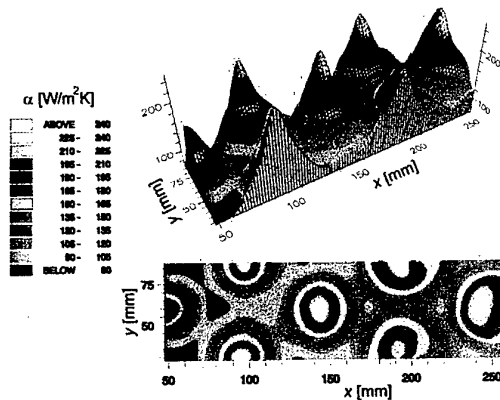
Figure 13 Detailed heat transfer coefficients on the target plate beneath an engine representative array of impinging jets. The flow exits from one side of the channel in the direction of the arrow.
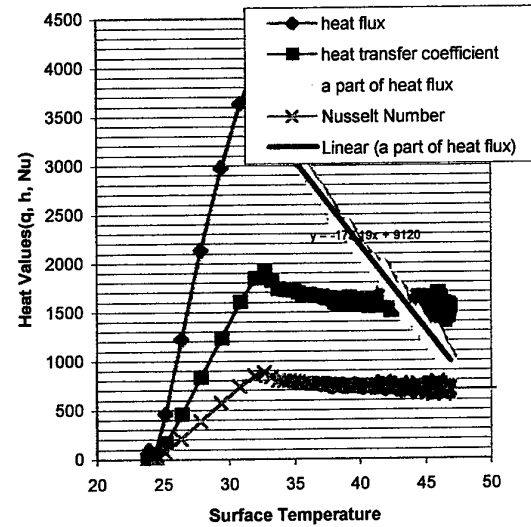
Figure 15 Heat flux versus surface temperature.
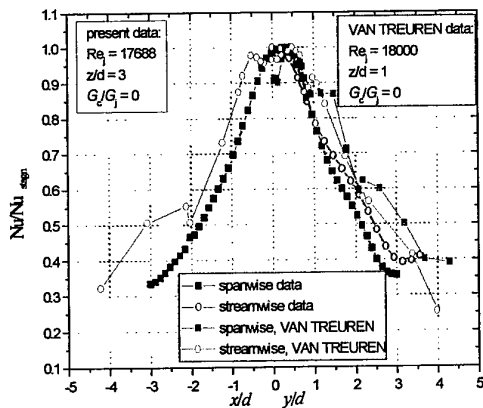
Figure 14 Comparison of normalised heat transfer coefficient for impingement arrays with very different spacing.
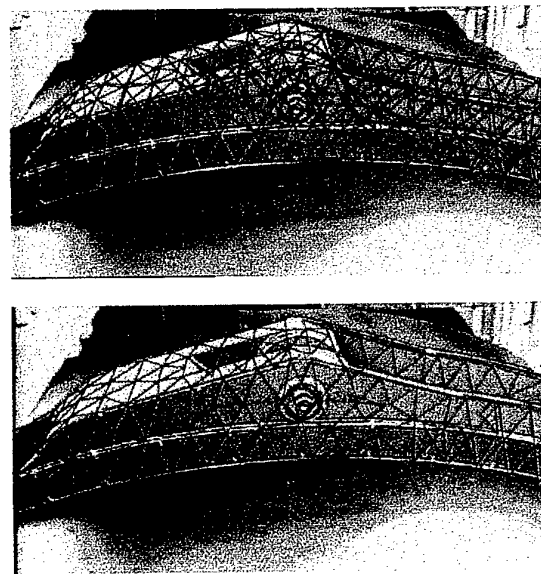
Figure 16 An example of the integration of a finite element software package with video images of a perspex model of an engine component. The lower figure has hidden lines removed.

8

Turbulent heat and mass transfer in a uniformly heated vertical tube with an ascending forced flow of air and a descending falling water film

P. An, J. Li and J.D. Jackson

School of Engineering, University of Manchester, UK

Abstract
Experimental and modelling studies are reported of combined heat and mass transfer to air flowing upwards within an electrically heated tube in the presence of a thin falling water film on the inside surface. Experiments were conducted to examine the influence of water injection temperature and water flow rate on the temperature distribution along the heated tube for several values of power input. A simple semi-empirical model was developed to simulate the experiments and enable the wall temperature distributions to be computed. The results yielded by the model proved to be in reasonable agreement with experiment. They indicate that when the water is supplied at near ambient temperature, the dominant mechanism of heat removal is convection by the cooling water. When the water is supplied at temperatures of 55°C and above, the dominant cooling mechanism is associated with evaporation of vapour from the free surface of the falling water film.

1. Introduction

In the case of passive cooling, fluid is induced naturally through a system simply as a result of heat transfer taking place rather than by the action of a pump or a fan. Due to the low flow rates which are typical of passively cooled systems the convective heat transfer process can be very different from that of forced convection. Depending on the thermal conditions and the geometry of the system, there could be strong interactions between free and forced convection. One of the characteristics of such mixed convection is that in heated upward flow the effectiveness of heat transfer may be seriously impaired as a result of turbulence production being reduced by buoyancy influences [1]. In a recent experimental study of this problem, Li [2] has shown that such conditions can certainly be encountered in a passively cooled system.

One apporach which has been proposed to overcome the problem of impaired heat transfer, is to enhance cooling by allowing a thin film of water to run down the heated surface. Under certain conditions, a considerable increase of heat removal can result from the evaporation of water at the free surface of the falling water film. Heat and mass transfer into the upward flowing mixture of air and vapour take place simultaneously.

In the present study, experiments have been conducted to examine the enhancement of cooling by this means. The system tested consisted of a uniformly heated vertical tube with a forced flow of air ascending inside it at known flow rates (typical of what might be achieved with naturally induced flow). Modelling studies have been undertaken in conjunction with the experiments. A simple semi-empirical model has been developed to simulate the heat and mass transfer processes involved. Computational studies using the model have enabled a better understanding to be gained of the relative importance of the various mechanisms of heat transfer involved.

2. The experimental investigation

2.1 Experimental apparatus

Figure 1 shows the arrangement of the test facility. The test section was a stainless steel tube, of internal diameter 76 mm, wall thickness 1.9 mm and length 8 m. The tube wall was resistively heated by passing electric current through it. The power was supplied by a variable voltage AC supply system. The outside of the tube was covered with a thick layer of thermal insulation and the heat generated within the tube wall was removed by means forced upward flow of air within the tube and a falling film of water running down the inside surface of the tube. The wall temperature distribution was measured by thermocouples attached to the outside surface of the tube at numerous axial locations. At the top of the test section, water could be sprayed uniformly onto the inside surface of the tube from a centrally positioned multi-jet nozzle. This could be supplied with water at chosen values of flow rate and temperature. The water was pre-heated by means of electrical immersion heaters in the water supply line. Its flowrate was measured using a rotameter. Air from a compressor was supplied to an entry box which enclosed the bellmouth intake at the bottom of the tube. The flow rate of air was monitored using a carefully calibrated flowmeter installed in the supply line.

2.2 Experimental conditions and procedure

The experimental conditions covered were as follows:

Electrical power input: 1,35, 3,00, 4,00 and 5,00 kW
Air flow rate: 0.005, 0.010 and 0.015 kg/s
Water injection rate: 0, 0.013 and 0.027 kg/s
Water injection temperature: 20, 40, 55 and 70 °C

Air was supplied to the test section at a temperature of 20°C. The Reynolds number at inlet corresponding to the three quoted air flow rates were

4600, 9200 and 13800.

In a typical test with water film cooling, a steady forced flow of air was pumped through the test section at the required rate and injection of water via the spray nozzle was commenced. Once a steady and uniform water film had been established, electrical heating was applied to the test section at a constant rate. The tests ran for a lengthy period, during which time the temperature distribution along the tube was monitored at regular intervals until a steady state condition had been achieved. Some tests were conducted without any water being supplied.

2.3 Presentation and discussion of experimental results

Figure 2 shows tube wall temperature distributions for three different air flow rates (0.015, 0.010 and 0.050 kg/s) under dry conditions with a power input of 1350 W. At the lowest flow rate the tube reached a temperature of 300°C near the top. This was the arbitrarily chosen operating temperature limit imposed to avoid damaging the test section. In that test, the conditions were such that influences of buoyancy were strong and the effects of non-uniformity of fluid properties significant. Some effect of buoyancy is evident from the shape of the tube wall temperature distribution which is irregular. Figure 3 shows the corresponding distribution of tube wall temperature for a flow rate of 0.015 kg/s with a power input of 3000 W. This also reached the operating temperature limit of 300°C and so, tests with the dry condition were not performed at lower air flow rates at that power. The results shown in Figure 2 and 3 provide a base against which data obtained with water film cooling can be compared. Figure 4 shows such comparisons for an air flow rate of 0.015 kg/s with a power input of 1350W. Results are presented there for two different water flow rates (13 g/s and 27 g/s) and four values of inlet water temperature, (a) 20°C, (b) 40°C, (c) 55°C and (d) 70°C. It can be seen that in each case water film cooling causes tube wall temperature to be greatly reduced. However, the behaviour changes with markedly increase of inlet water temperature.

From Figure 4(a), it can be seen that at the lowest value of water temperature at inlet (20°C), the water first increases in temperature as it descends and then its temperature begins to fall. As one would expect, the rate at which it increases in temperature is greater in the case of the lower water flow rate because the heat input from the tube to the water film is essentially the same for both flow rates. The fall of temperature of the descending water is brought about by evaporation of water from the surface of the film. The latent heat needed is obtained at the expense of the internal energy of the water left behind. The rate of evaporation is very sensitive to the temperature of the water because saturation vapour pressure increases strongly with temperature. Therefore, evaporation builds up where the temperature of the water rises as it descends down the upper part of the tube. Once the effect of heat removal due to evaporation becomes greater than the heat input

to the water film from the tube, the temperature of the descending water begins to fall. The changeover occurs earlier in the case of the test with the lower water flow rate because, in that case, the water temperature is higher due to the rise of temperature in the upper part of the tube being greater. The water leaving the bottom of the test section is hotter that that injected at the top. Most of the heat generated in the tube wall is carried away by the water leaving the test section. The air/vapour mixture, which rises up the tube increasing in temperature leaves at the top carrying some heat with it. In the upper part of the tube the conditions are such that some of the ascending vapour is likely to condense onto the water film releasing heat as it does. This would increase the temperature rise of the descending water. We see that a variety of heat transfer mechanisms and some rather complicated processes can be involved in experiments with water film cooling.

Referring next to Figure 4(b), water temperature at inlet 40°C, we see that the behaviour is rather different. The temperature of the descending water changes much less. A small net rise of temperature occurs in the case of the high water flow rate and there is a small decrease in the case of the lower water flow rate. Evaporation of the water film is important over the whole length of the tube because the water temperature in this case is everywhere approximately 40°C. As one would expect, the extent to which the water is cooled as it falls is greater in the case of the lower water flow rate so the two distributions of tube wall temperature do diverge slightly in the lower part of the test section Generally, however, the influence of water flow rate on tube wall temperature distribution is quite small.

Figure 4(c) shows results for a water temperature at inlet of 55°C. The trend in terms of the increasing importance of evaporation with increase of inlet water temperature is continued. For both of the water flow rates, the effect of evaporation is that the descending water undergoes a steady fall in temperature. Again, the rate at which this occurs is greater for the lower water flow rate. The air/vapour mixture leaves the top of the test section not only taking with it the electrical energy generated within the tube wall but also heat which has been released by the descending water film.

Finally, we consider the results shown in Figure 4(d) for the highest inlet water temperature (70°C). Here, evaporation is of even greater importance. A steep fall in the temperature of the descending water film is very evident, particularly near the top of the test section where the temperature of the water is highest. Again, the effect is greatest in the case of the test with the lower water flow rate.

Figure 5 shows a corresponding set of results for a lower air flow rate (0.01 kg/s) and the same power input (1350 W). The general picture is very similar, particularly for the lower values of water temperature at inlet (20°C and 40°C). For water temperature of 55°C and 70°C, the tube wall temperatures are slightly higher than the corresponding ones shown in Figure 4, a consequence of the effectiveness of heat and mass transfer into the air/vapour being less with the lower air

flow rate. However, the effect is quite small and main result of reducing the air flow rate is that the influence of water flow rate is reduced for values of inlet water temperature of 40°C and above. The results shown in Figure 5 generally follow a similar pattern to those in Figure 4.

Figures 6,7,8 and 9 show the influence of air flow rate on tube wall temperature distribution for inlet water temperatures of 20°C, 40°C, 55°C and 70°C. with a power input of 1350W. Three values of air flow rate are covered in each case.

For a water temperature at inlet of 20°C (Figure 6), it can be seen that air flow rate only affects the heat transfer process in the lower part of the tube. There, evaporation from the descending water film is important. The tube wall temperature needs to be higher in the case of the lower air flow rate to transfer heat by turbulent convection from the water film into he air/vapour mixture. The effect is most apparent at the lowest air flow rate of 0.005 kg/s where some buoyancy induced impairment of turbulent diffusion is beginning to be experienced. This is of importance in the case of the corresponding results for inlet water temperatures of 40°C, 55°C and 70°C, shown in Figure 7,8 and 9. The heat transfer mechanisms present in the cases shown in Figures 6 to 9 are essentially the same as those discussed earlier with the added influence of buoyancy at the lowest air flow rate.

We next consider the effect of increasing the power input to the test section. Figures, 9, 10 11 and 12 together provide a picture of what happens as power input is increased in the range of 1350 W to 5000 W for a fixed value of inlet water temperature of 70°C. Three air flow rates are covered in each case (0.005 kg/s, 0.010 kg/s and 0.015 kg/s). The most striking feature of this series of results is that the tube wall temperature only increases by a rather modest amount as a consequence of the power being increased by a factor of over three. The peak wall temperature with a power input of 5000 W is only 82°C, as compared with 72°C for a power input of 1350 W. In each ease the dominant mechanism for heat removal from the tube is evaporation of water from the descending water film. The turbulent convection process is rather dependant on air flow rate and a systematic increase of wall temperature is evident in each case as this is reduced. In all cases, not only is heat removed from the tube but also the falling water is cooled down by a significant amount. The system is, in effect, operating as an evaporative cooler. In Figure 13 the results for a power input 3000 W are presented again. However, this time they are plotted on a different scale along with the tube wall temperature distribution for dry conditions. This figure highlights the effectiveness of evaporation from a falling water film as a mechanism for heat. It is apparent that without water film cooling the tube wall temperature would have been greatly in excess of 300°C for power inputs of 4000 W and 5000 W and serious overheating of the test section would have occurred. However, using water film cooling with water at 70°C, the tube is maintained at a perfectly acceptable temperature which is actually below that of the cooling water.

3. The modelling study

3.1 Physical system

In the modelling study. it was assumed that the tube was uniformly heated and perfectly insulated on the outside. A circumferentially uniform film of water flowed downwards on the inside surface of the tube under the action of gravity. Water at temperature $T_{l,0}$ is supplied at the top of the tube at a flow rate of mf_l. Air is supplied to the tube at the bottom with a mass flow rate mf_a at temperature $T_{g,0}$ with relative humidity Rh.

3.2 The modelling approach

The test section is divided into N elements along its length (see Figure 14). Each element is made up of three regions, the *wall*, *liquid film* and *gas flow* regions. The variables for each element (see Figure 15) are the tube wall temperature $T_{w,i}$, the gas temperature $T_{g,i}$, the concentration of vapour in the gas stream $d_{v,i}$ and the gas velocity $V_{g,i}$. The input parameters are the power input Q, the initial water film temperature (i.e. water injection temperature) $T_{l,0}$ ($=T_{w,N}$), the water injection flow rate mf_l, the air flow rate mf_a, the air inlet temperature $T_{g,0}$ and air inlet relative humidity Rh. The mass and energy balance equations involving these variables and parameters are formulated for each of the three regions. The rate of convective heat transfer from the water film to the gas stream at the water-air interface is calculated using a well-established empirical correlation [3] with account being taken of the effect of buoyancy influences [2]. The rate of mass transfer is calculated by making use of the heat/mass transfer analogy. Then, with the boundary conditions specified, the tube wall temperature, the bulk temperature of gas and other parameters can be computed.

3.3 Modelling results

Figures 16 to 19 show the temperature distributions for a fixed water injection rate of 0.027 kg/s and a fixed water temperature of 70°C for four power inputs (1350, 3000, 4000 and 5000 W).

In each figure, the three sets of experimental data (denoted by markers) correspond to mass flow rates of air through the system of 0.005, 0.010 and 0.015 kg/s. The corresponding wall temperature distributions obtained using the the semi-empirical model are shown by full and broken lines.

3.4 Discussion of the modelling results

It can be seen that the semi-empirical model reproduces the experimentally observed behaviour extremely well for the cases shown. Quite good agreement was also obtained in the case of experiments with water temperature at inlet of 55°C. Agreement between the predicted results and experiment for water temperatures at inlet of 40°C and 20°C is less satistactory but nevertheless the main trends exhibited by the

experimental data are still reproduced quite well.

There are three mechanisms involved in the cooling process, namely, *laminar convection in the descending water film, turbulent convection of heat in the upward flow of air and vapour* and *evaporation of the water film*. The numerical simulations enable us to evaluate the separate contributions to overall heat removal. Figure 20 shows a breakdown of heat transfer to the water to the air/vapour mixture for experiments with a power input of 1350 W for the various values of water temperature at inlet. Figure 20(a) shows the rate of heat removal due to laminar convection by the water. With low water injection temperatures (20 and 40°C), the removal rate is positive, i.e. the falling water film carries heat away with it. With higher water injection temperatures (55 and 70°C), the value is negative. The descending water film leaves the test section colder than when it was injected. Figure 20(b) shows separately the rates of heat removal due to turbulent heat convection in the mixture and evaporation. Generally, both get bigger with increase in water injection temperature. It can be seen that, the rate of heat removal due to evaporation is much higher than that due to turbulent convection in the mixture. This confirms that evaporation plays a dominant role in the overall cooling process for such conditions. From Figures 20(a) and 20(b), we can see in detail how the contributions of these heat transfer mechanisms vary with the water injection temperature. For example, consider an air flow rate of 0.005 kg/s, a water flow rate of 27 g/s and a power input of 1350 W. The percentage contributions of the individual mechanisms to the overall heat removal are as tabulated below.

Table 1 Percentage heat removal by laminar convection in the falling water film, turbulent convection of heat in the air/vapour mixture and evaporation

Water injection temperature	Laminar convection by falling water film	Turbulent convection of heat in mixture	Evaporation from the water film
20°C	90%	1%	9%
40°C	43%	9%	48%
55°C	-5%	12%	93%
70°C	-117%	18%	199%

We see that with the lowest water injection temperature of 20°C, heat removal by the flowing water represents 90 percent of the overall heat removal. Evaporation contributes only 9 percent. This pattern changes, however, as the water injection temperature is increased. For the highest water injection temperature of 70°C, the falling water film does not remove any heat, in fact it releases a considerable amount. A lot of heat is removed as a result of evaporation. The percentage of heat removal by turbulent convection of heat is much lower and varies from 1% to 18%.

Figures 21(a) and 21(b) show the rate of heat removal by the three mechanisms as a function of power input and air flow rate for a water injection rate of 0.027 kg/s and a water temperature of 70°C at inlet. It can be seen that evaporation is in all cases the dominant mechanism of heat removal.

The modelling study reported hear has enabled a very useful picture to be obtained of the extent to which the various   mechanisms of heat transfer contribute to the removal of heat.

4. Conclusions

The application of water film cooling substantially reduces tube wall temperature as compared to that for air flow alone. Three mechanisms are involved, namely, laminar convection in the descending water film, turbulent convection of heat in the upward flow of air and evaporation from the water film into the air/vapour mixture. The experimental and modelling studies reported here have shown that with water injection at the higher temperatures used in the tests (55°C and 70°C) evaporative heat transfer is the dominant heat removal mechanism. With low power levels and low inlet water temperature, the principal cooling mechanism is laminar convection in the descending water film.

References

[1] J.D., Cotton M.A. and Axcell B.P. `Review: tudies of mixed convection in vertical tubes', International Journal of Heat and Fluid Flow, 1989, vol 10, 2-15

[2] Li J. `Studies of Buoyancy-Influenced Convective Heat Transfer to Air in A Vertical Tube', PhD Thesis, University of Manchester, 1994.

[3] Petukhov, B.S. and Kurganov, V.A. and Gladuntsov, A.I., Turbulent heat transfer in tubes to gases with variable physical properties. Heat and Mass Transfer, Vol.1, pp.117-127, Izd. ITMO AN BSSR, Minsk (in Russian), 1972.

Acknowledgement

Water supply

Water sprayer

Water spray

Stainless steel test section pipe
76 mm diameter and 1.9 mm wall thickness

Thermal insulation

8 m

Step-down transformer

Variac

Electrical supply

Air entry box

Forced flow of air from compressor

Bellmouth intake

Water drain arrangement
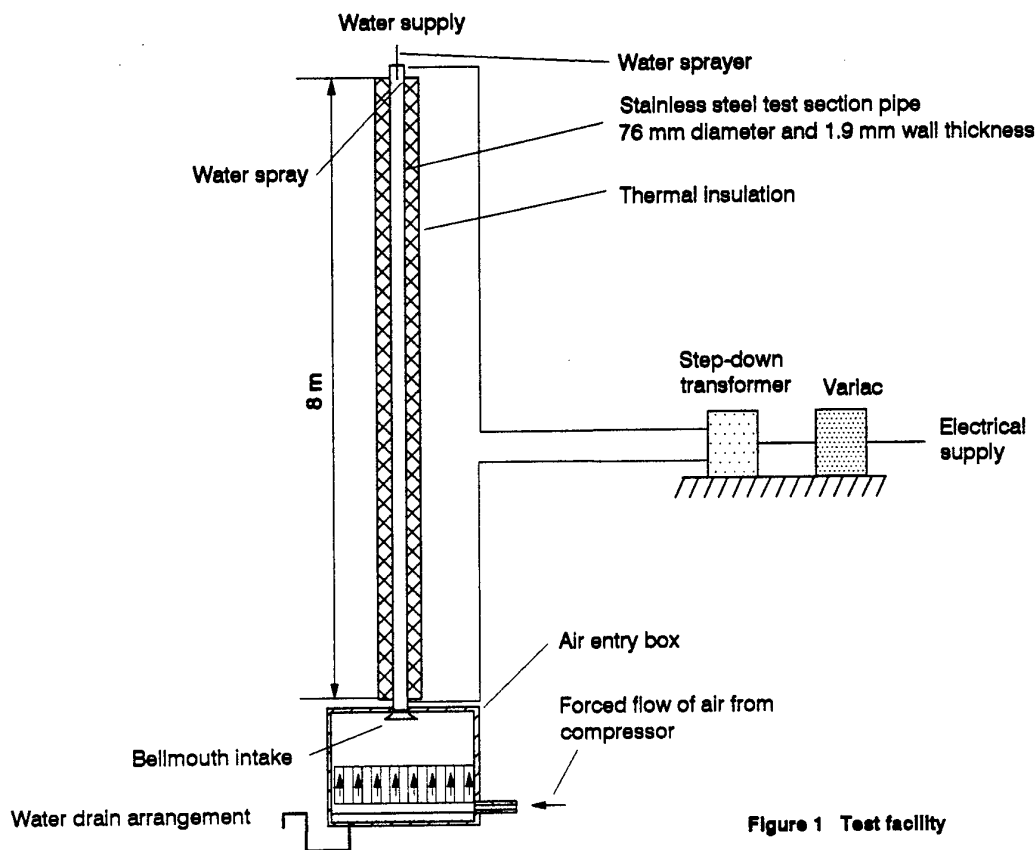
Figure 1 Test facility

Power input: 1350 W
Air inlet temp: 20 deg C

Air flow rate: 0.015 Kg/s

Air flow rate: 0.010 Kg/s

Air flow rate: 0.005 Kg/s

Wall temperature (deg C)

Distance from the bottom of the tube (m)

Figure 2 Tube wall temperature distribution under dry conditions

Power input: 3000W
Air inlet temp: 20 deg C

Air flow rate: 0.015 Kg/s

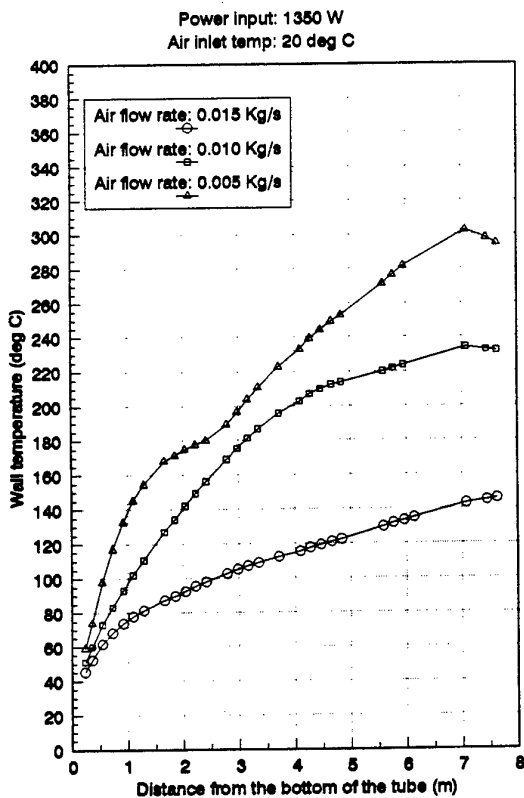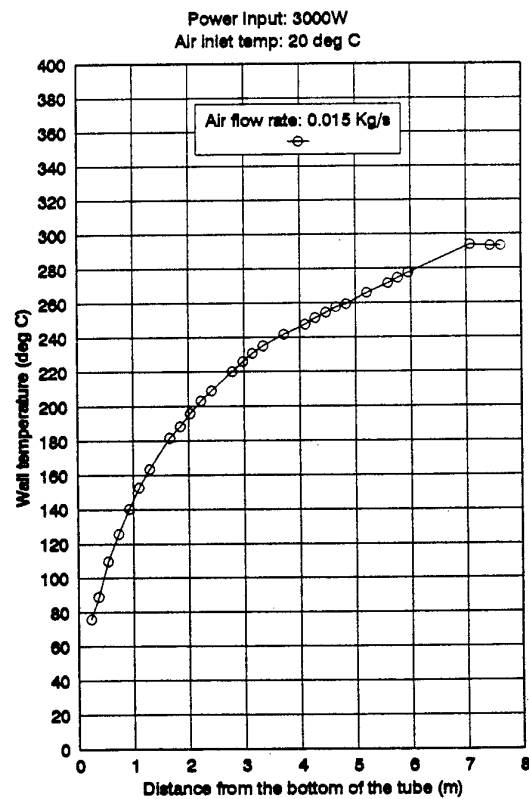Wall temperature (deg C)

Distance from the bottom of the tube (m)

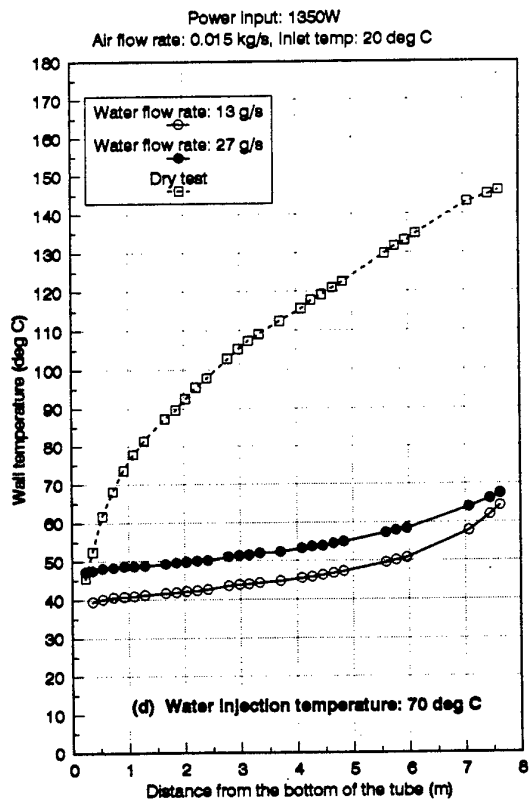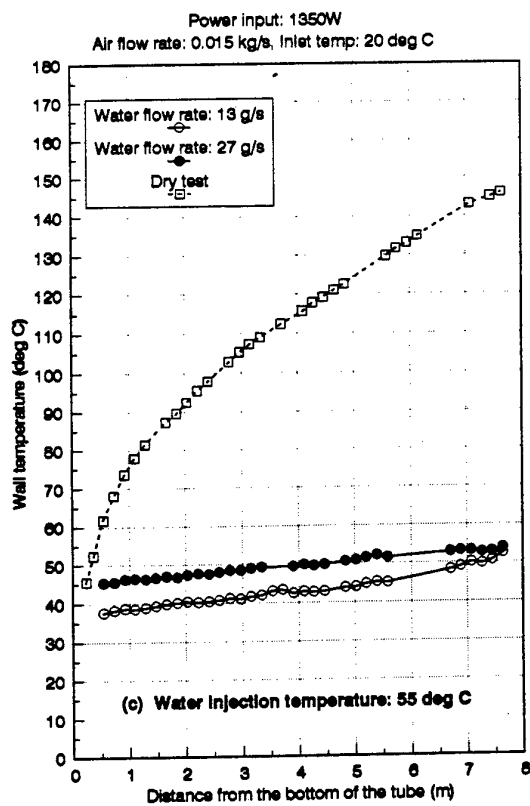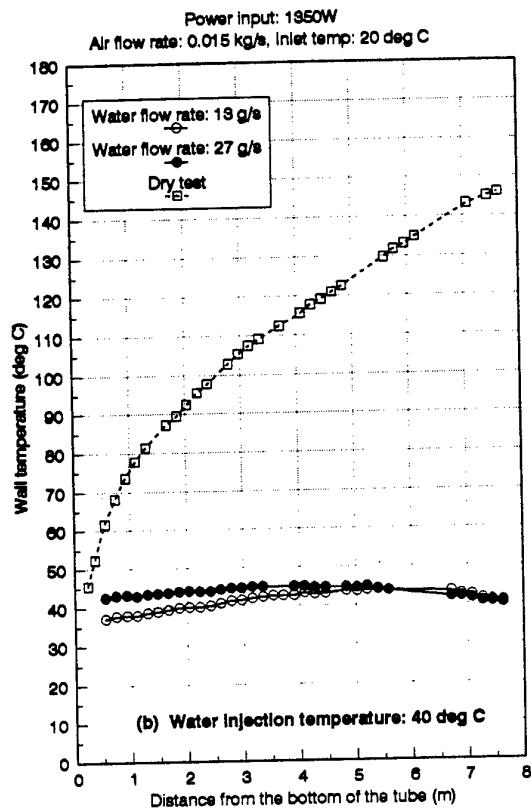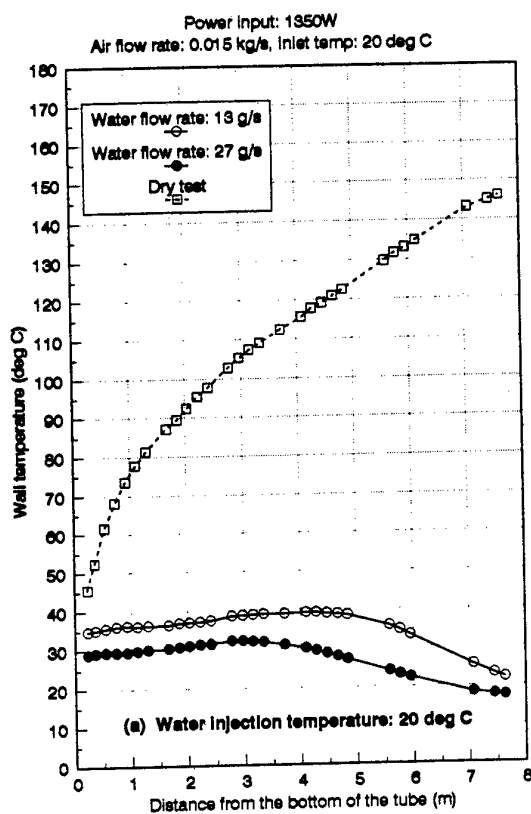**Figure 3 Tube wall temperature distributions under dry conditions**

Figure 4 Tube wall temperature distributions with water film cooling

Figure 5 Tube wall temperature distributions with water film cooling

Power input: 1350 W
Water flow rate: 27 g/s, Water temp: 20 deg C
Air inlet temp: 20 deg C

Air flow rate: 0.015 kg/s
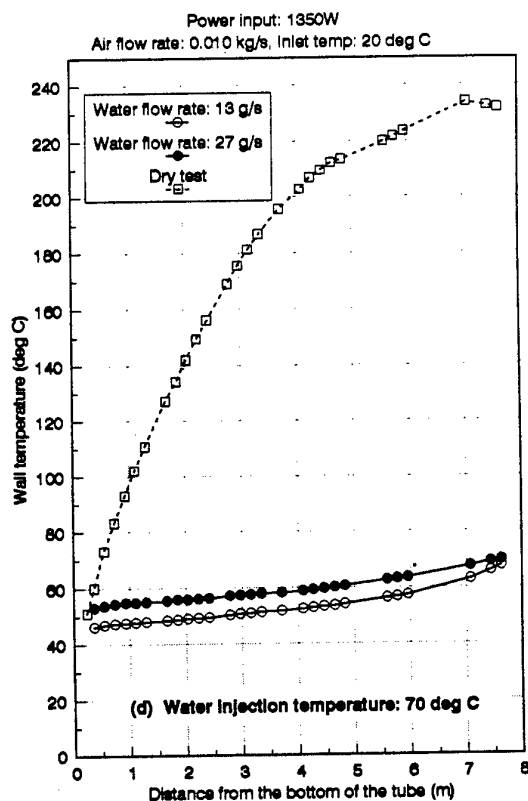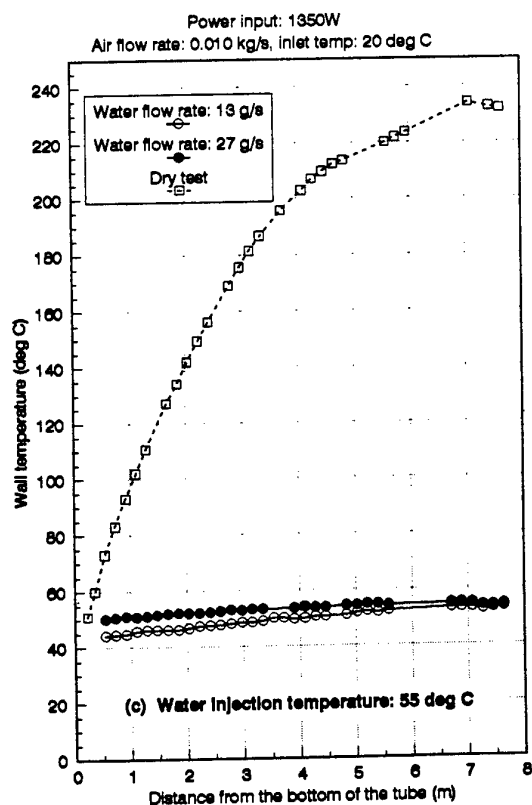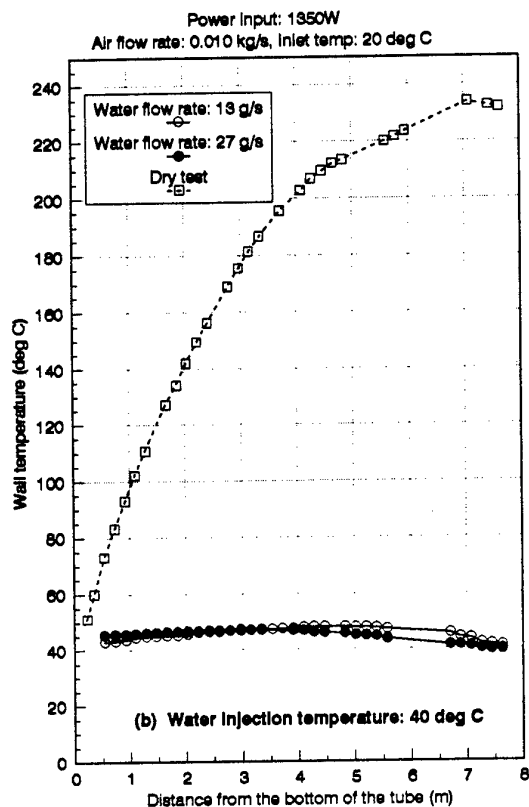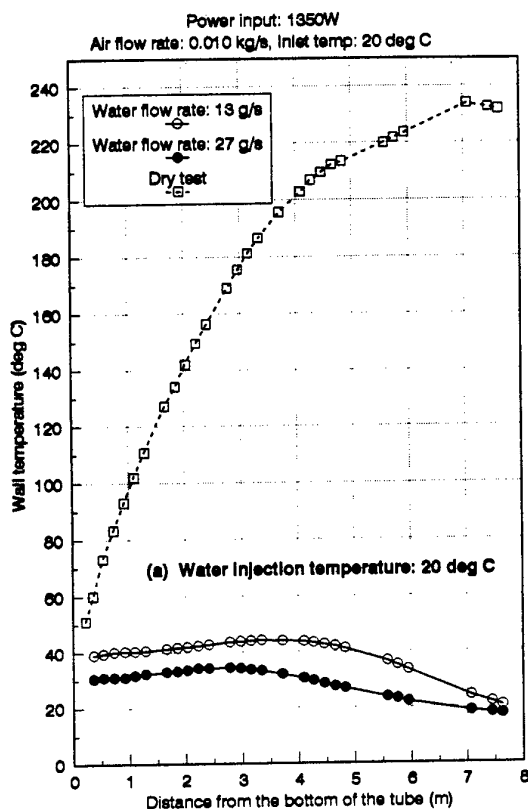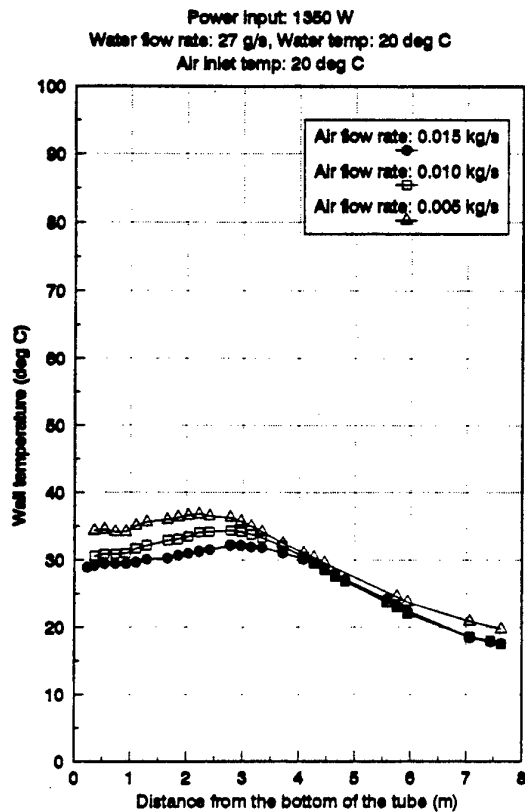Air flow rate: 0.010 kg/s
Air flow rate: 0.005 kg/s

Figure 6 Tube wall temperature distributions with water film cooling

Power input: 1350 W
Water flow rate:27 g/s, Water temp: 40 deg C
Air inlet temp: 20 deg C

Air flow rate: 0.015 kg/s
Air flow rate: 0.010 kg/s
Air flow rate: 0.005 kg/s
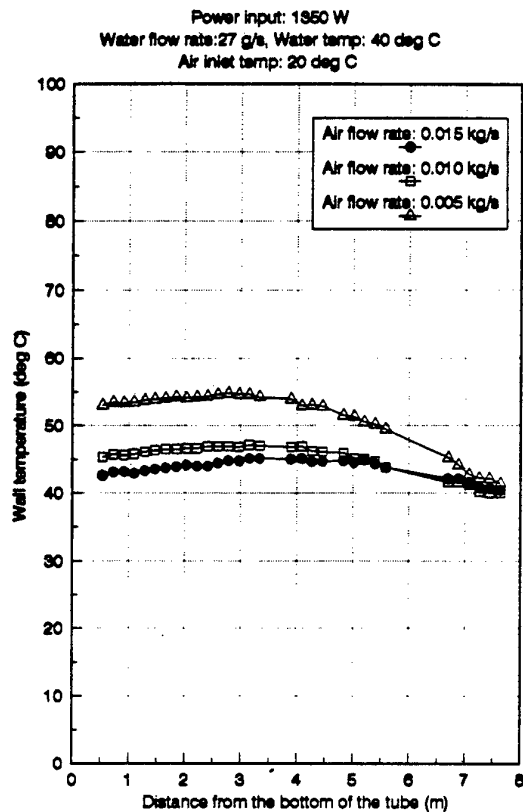
Figure 7 Tube wall temperature distributions with water film cooling

Power input: 1350 W
Water flow rate:27 g/s, Water temp: 55 deg C
Ambient temp: 20 deg C

Air flow rate: 0.015 kg/s
Air flow rate: 0.010 kg/s
Air flow rate: 0.005 kg/s
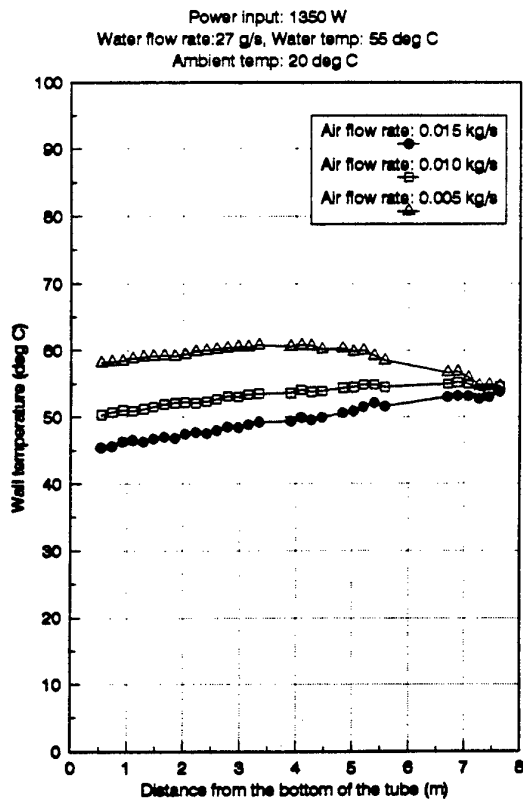
Figure 8 Tube wall temperature distributions with water film cooling

Power input: 1350 W
Water flow rate: 27 g/s, Water temp: 70 deg C
Air inlet temp: 20 deg C

Air flow rate: 0.015 kg/s
Air flow rate: 0.010 kg/s
Air flow rate: 0.005 kg/s
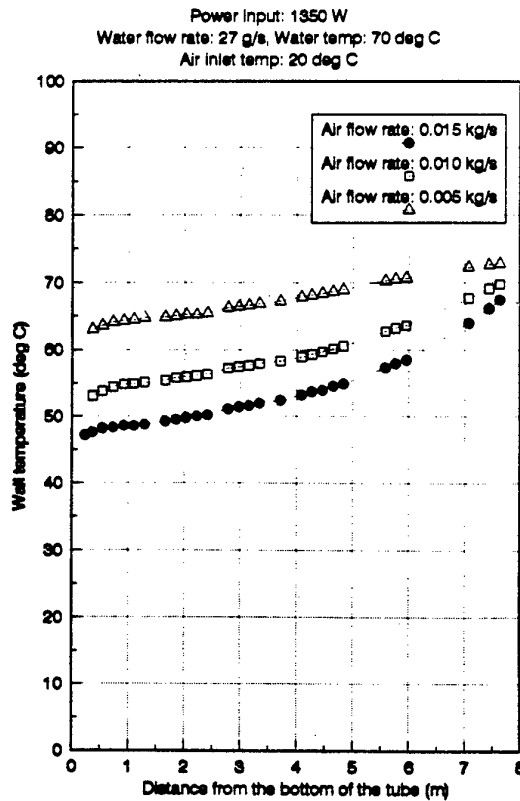
Figure 9 Tube wall temperature distributions with water film cooling

Power input: 3000 W
Water flow rate: 27 g/s, Water temp: 70 deg C
Air inlet temp: 20 deg C
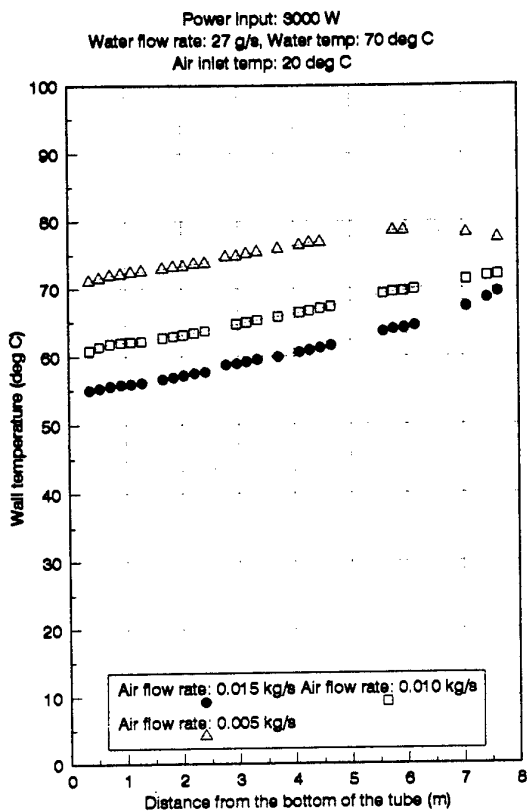
Figure 10 Tube wall temperature distributions with water film cooling

Power input: 4000 W
Water flow rate:27g/s, Water temp: 70 deg C
Air inlet temp: 20 deg C
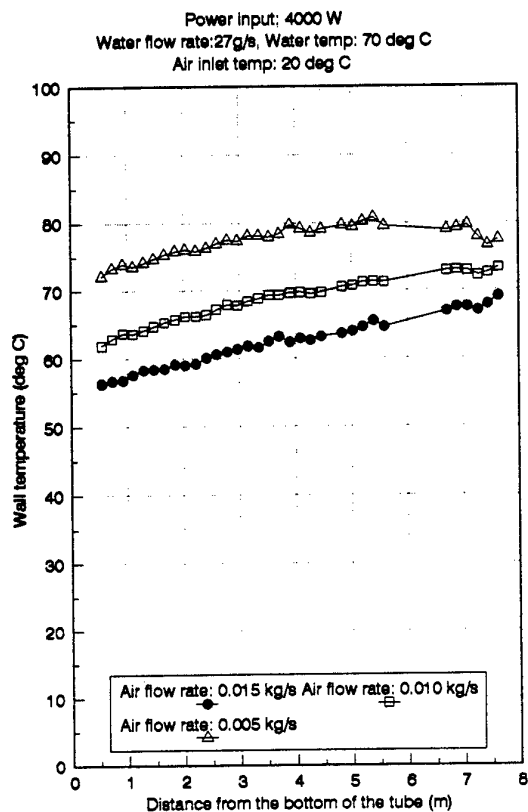
Figure 11 Tube wall temperature distributions with water film cooling

Power input: 5000 W
Water flow rate:27g/s, Water temp: 70 deg C
Air inlet temp: 20 deg C
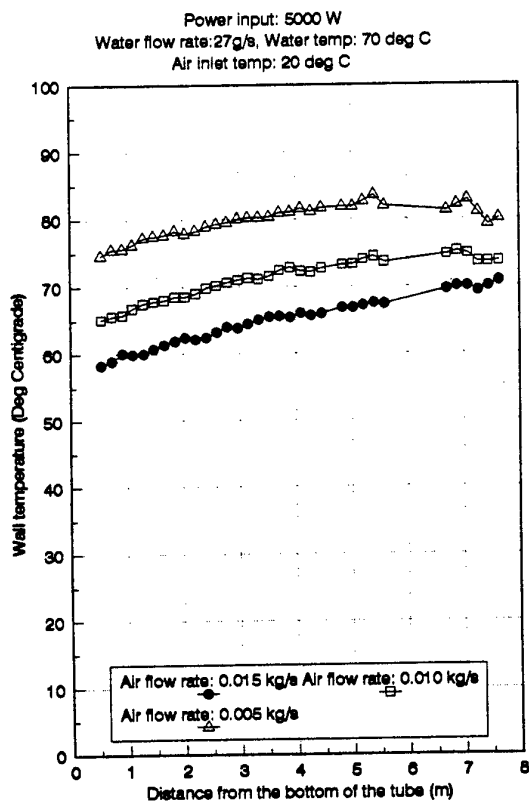
Figure 12 Tube wall temperature distributions with water film cooling

Power input: 3000 W
Water flow rate: 27 g/s, Water temp: 70 deg C
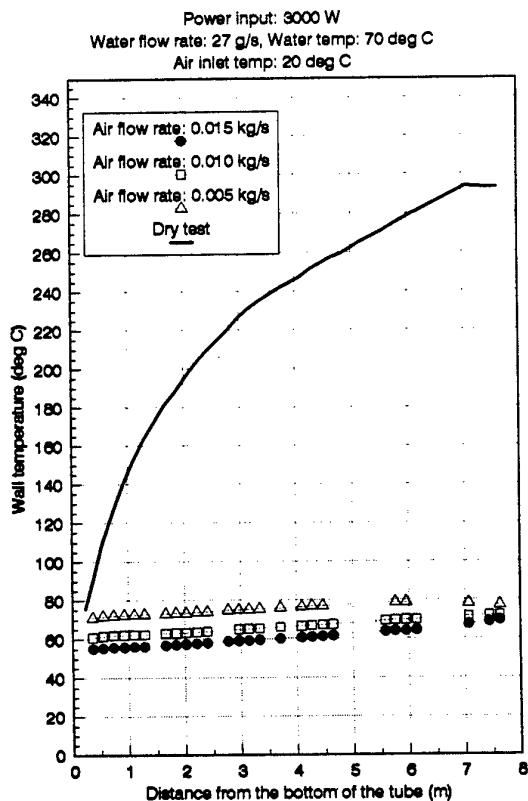Air inlet temp: 20 deg C

Figure 13 Tube wall temperature distributions
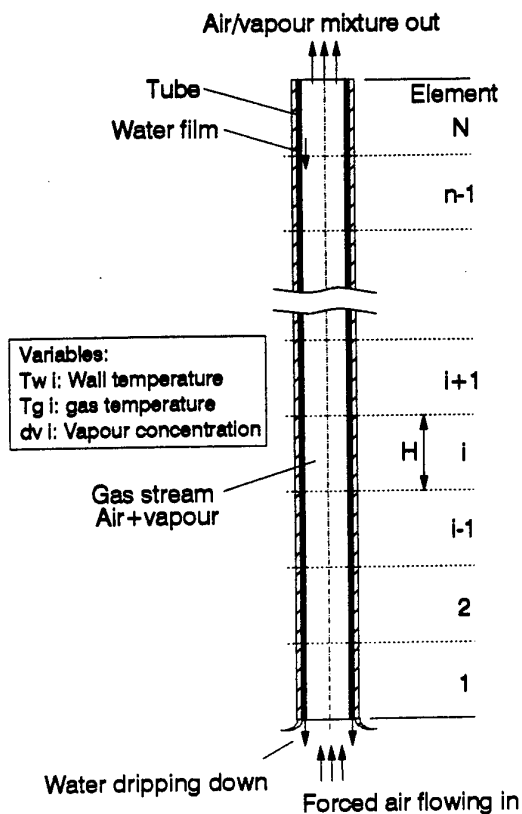
Figure 14 Modelling details
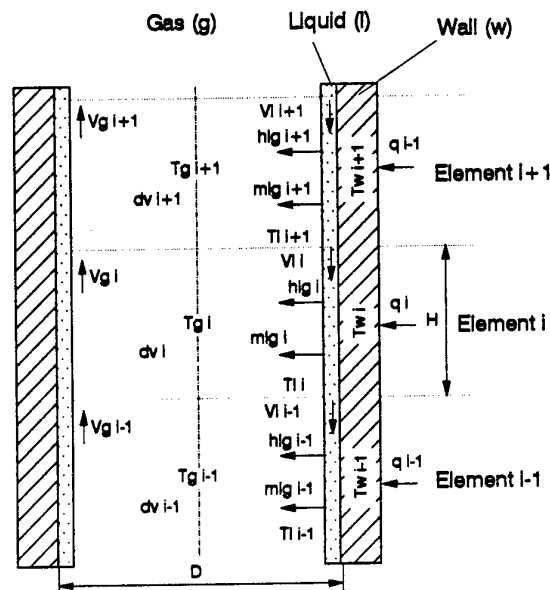
Figure 15 Parameters and variables for element i-1, i and i+1

Power input: 1350 W
Water flow rate: 27 g/s, Water temp: 70 deg C
Air inlet temp: 20 deg C

Air flow rate: 0.015 kg/s
Experiments   Model
●

Air flow rate: 0.010 kg/s
Experiments   Model
□

Air flow rate: 0.005 kg/s
Experiments   Model
△

Figure 16 Comparison of predicted tube wall temperature
distributions with experimental results

Power input: 3000 W
Water flow rate: 27 g/s, Water temp: 70 deg C
Ambient temp: 20 deg C

Air flow rate: 0.015 kg/s
Experiments   Model
●

Air flow rate: 0.010 kg/s
Experiments   Model
□

Air flow rate: 0.005 kg/s
Experiments   Model
△

Figure 17 Comparison of predicted tube wall temperature
distributions with experimental results

Power input: 4000 W
Water flow rate:27g/s, Water temp: 70 deg C
Ambient temp: 20 deg C

Power input: 5000 W
Water flow rate:27g/s, Water temp: 70 deg C
Ambient temp: 20 deg C

Air flow rate: 0.015 kg/s
Experiments   Model
●
Air flow rate: 0.010 kg/s
Experiments   Model
□   - - - -
Air flow rate: 0.005 kg/s
Experiments   Model
△

Wall temperature (deg C)
Distance from the bottom of the tube (m)

Air flow rate: 0.015 kg/s
Experiments   Model
●
Air flow rate: 0.010 kg/s
Experiments   Model
□   - - -
Air flow rate: 0.005 kg/s
Experiments   Model
△

Wall temperature (deg C)
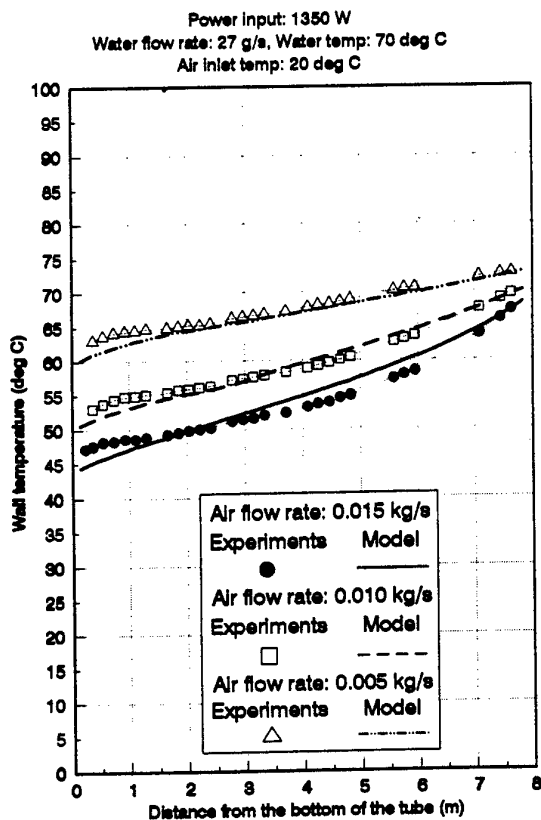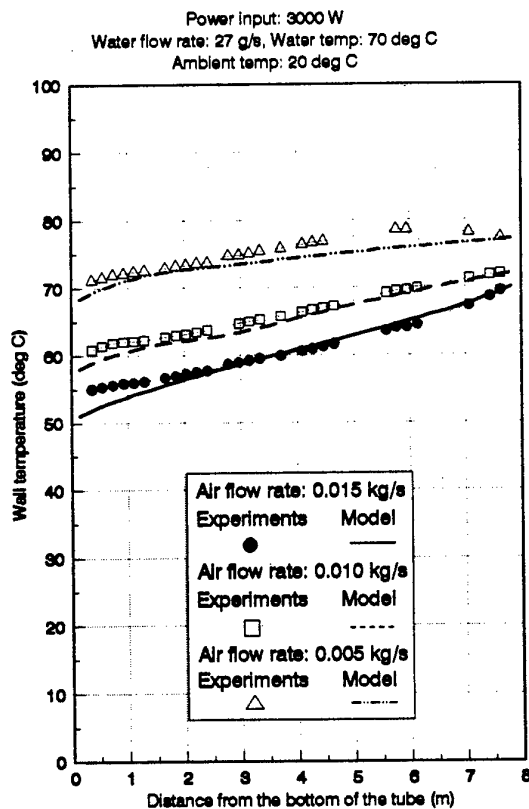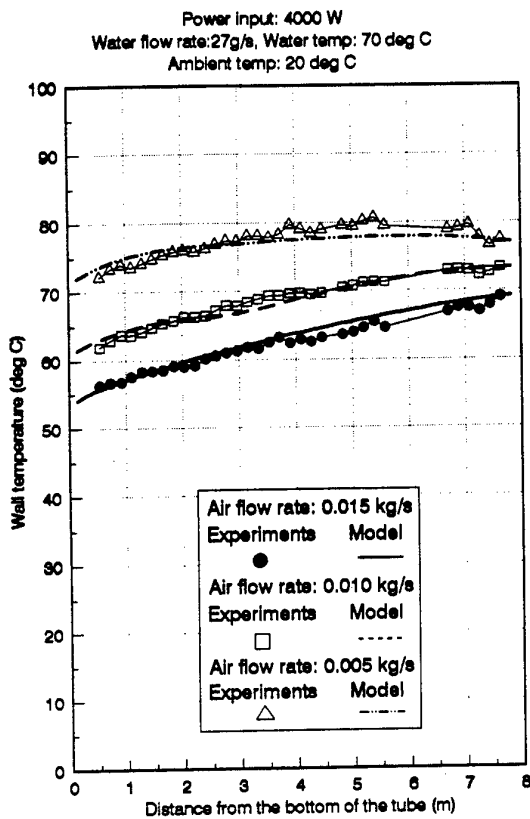Distance from the bottom of the tube (m)

Figure 18 Comparison of predicted tube wall temperature distributions with experimental results

Figure 19 Comparison of predicted tube wall temperature distributions with experimental results
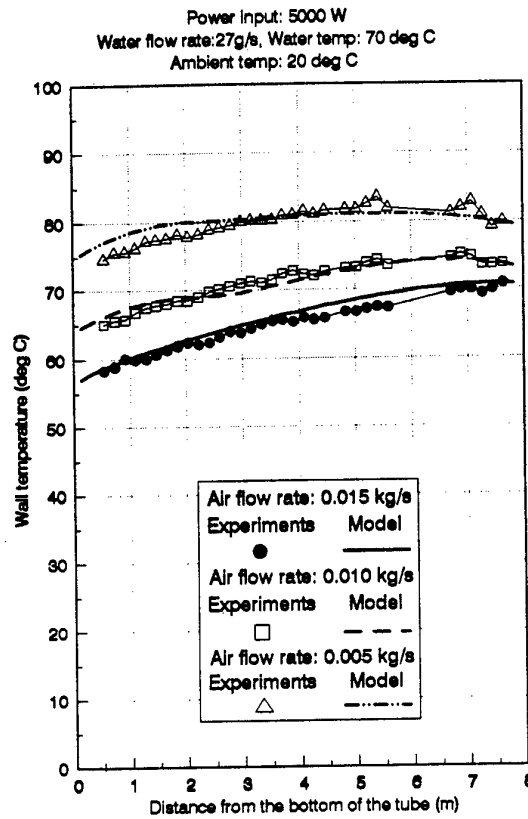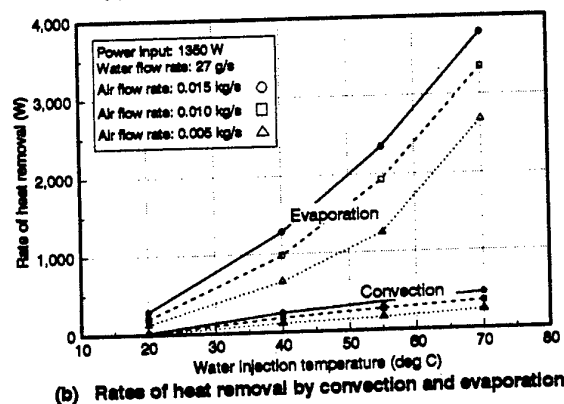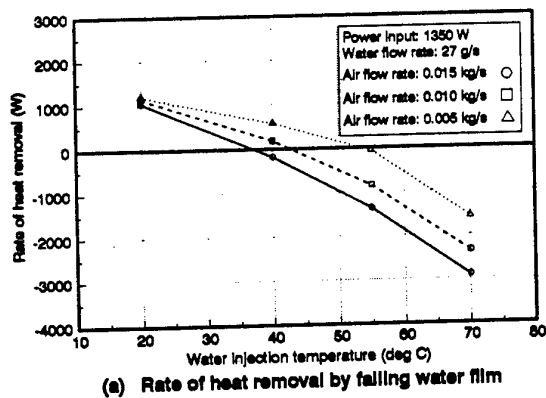
Power input: 1350 W
Water flow rate: 27 g/s
Air flow rate: 0.015 kg/s ○
Air flow rate: 0.010 kg/s □
Air flow rate: 0.005 kg/s △

Rate of heat removal (W)
Water injection temperature (deg C)

(a) Rate of heat removal by falling water film

Water flow rate: 27 g/s   Water temp: 70 deg C
Air flow rate: 0.015 kg/s ○   Air flow rate: 0.010 kg/s □
Air flow rate: 0.005 kg/s △

Rate of heat removal (W)
Electrical power input (W)

(a) Rate of heat removal by the falling water film

Power input: 1350 W
Water flow rate: 27 g/s
Air flow rate: 0.015 kg/s ○
Air flow rate: 0.010 kg/s □
Air flow rate: 0.005 kg/s △

Evaporation
Convection

Rate of heat removal (W)
Water injection temperature (deg C)

(b) Rates of heat removal by convection and evaporation

Water flow rate: 27 g/s   Water temp: 70 deg C
Air flow rate: 0.015 kg/s ○   Air flow rate: 0.010 kg/s □
Air flow rate: 0.005 kg/s △

Evaporation
Convection

Rate of heat removal (W)
Electrical power input (W)

(b) Rates of heat removal by convection and evaporation
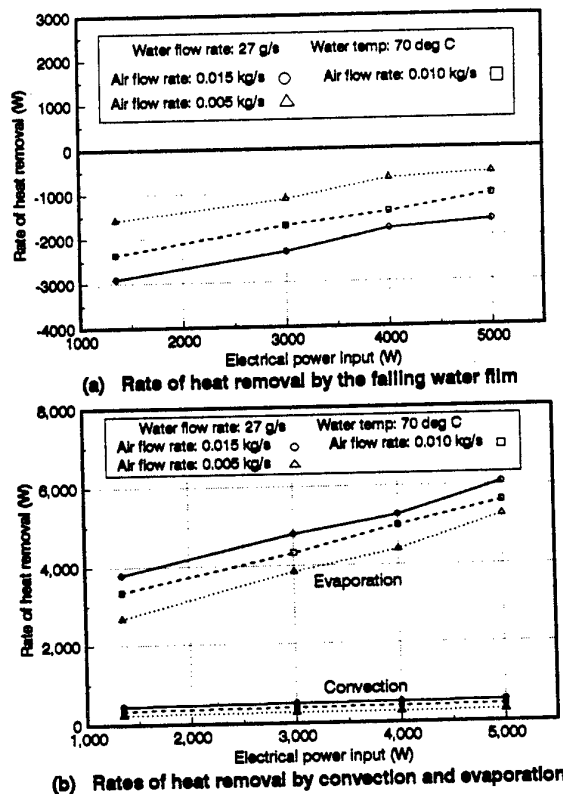
Figure 20 Contributions of heat transfer mechanisms

Figure 21 Contributions of heat transfer mechanisms